

# Demagnetization by basin-forming impacts on early Mars: Contributions from shock, heat, and excavation

Robert J. Lillis,<sup>1</sup> Sarah T. Stewart,<sup>2</sup> and Michael Manga<sup>3</sup>

Received 19 December 2012; revised 19 April 2013; accepted 21 April 2013; published 23 May 2013.

[1] Large hypervelocity impacts occurred frequently on ancient Mars, leaving many large impact basins visible today. After the planetary dynamo ceased operating, such impacts demagnetized the crust by way of (1) excavation of magnetized material, (2) heating, and (3) shock pressure. We investigate these three demagnetizing processes, both separately and in combination, using hydrocode simulations of large impacts on early Mars at a range of impact energies and using a new parameterization of the shock pressure-demagnetization behavior of candidate Martian minerals. We find that in general, shock pressure demagnetization is more important than thermal demagnetization, except in the combined case of very large impacts (more than  $\sim 10^{26}$  J) and low Curie temperature minerals such as pyrrhotite. We find that total demagnetized area has a power law dependence on impact energy (with an exponent of 0.6–0.72) and that depending on the magnetic mineral, the demagnetized area resulting for a given impact energy can vary over approximately an order of magnitude. We develop an empirical model that can be used to calculate total demagnetized area for a given impact energy and magnetic mineral (whose pressure-demagnetization properties are known). Once a reliable basin scaling law for ancient Mars (i.e., relating impact energy to final basin topography) is derived, this mineral parameterization and empirical model will allow robust constraints to be placed upon the primary Martian magnetic carrier(s).

**Citation:** Lillis, R. J., S. T. Stewart, and M. Manga (2013), Demagnetization by basin-forming impacts on early Mars: Contributions from shock, heat, and excavation, *J. Geophys. Res. Planets*, 118, 1045–1062, doi:10.1002/jgre.20085.

## 1. Introduction

### 1.1. Impacts and Their Relationship to Crustal Magnetization

[2] When a large hypervelocity impact occurs on a planetary body such as Mars, the kinetic energy of the impactor is partitioned primarily into (1) kinetic energy of the planetary crust and mantle as they deform and flow in response to the impact; (2) heating, melting, and vaporization of impactor, crust, and mantle material; and (3) shockwaves that travel throughout the entire volume of the planet [e.g., *Melosh*, 1989]. These processes alter the magnetization of the crust by way of (1) excavation and rotation of magnetized material, (2) thermal de(re-)magnetization, and (3) shock de(re-)magnetization, respectively.

[3] Following the impact, ferromagnetic minerals in the crust eventually cool below their magnetic blocking temperatures and acquire a thermoremanent magnetization (TRM) with a magnitude proportional to the strength of the ambient magnetic field and the capacity of the rock to carry thermoremanence. In addition, magnetic materials can be magnetized in an external magnetic field through shock remanent magnetization (SRM) and existing magnetization can be reduced or erased if the minerals are shocked in an ambient field too weak to induce a sufficient SRM [*Cisowski and Fuller*, 1978, *Gattacceca et al.*, 2007a, 2007b, 2010]. Brecciation and fluid circulation can combine to produce post-impact hydrothermal systems which can lead to further TRM (or lack thereof) and/or the acquisition of chemical remanent magnetization (CRM), the strength of which is controlled primarily by oxygen fugacity and cooling speed [*Stokking and Tauxe*, 1987]. Because Mars lacks a global, dynamo-driven magnetic field, essentially all magnetization is TRM, SRM, or CRM. By way of these processes, basin-forming impacts on Mars have altered the magnetization of the entire depth of crust over a geographic area roughly comparable to the final size of the impact basin [e.g., *Hood et al.*, 2003; *Shahnas and Arkani-Hamed*, 2007; *Louzada and Stewart*, 2009].

### 1.2. Magnetic Field History of Mars

[4] The strong crustal magnetic fields on Mars measured by Mars Global Surveyor (MGS) can only be explained by

<sup>1</sup>Space Sciences Laboratory, University of California, Berkeley, Berkeley, California, USA.

<sup>2</sup>Department of Earth and Planetary Sciences, Harvard University, Cambridge, Massachusetts, USA.

<sup>3</sup>Department of Earth and Planetary Sciences, University of California, Berkeley, Berkeley, California, USA.

Corresponding author: R. J. Lillis, Space Sciences Laboratory, University of California, Berkeley, 7 Gauss Way, Berkeley, CA 94720, USA. (rlillis@ssl.berkeley.edu)

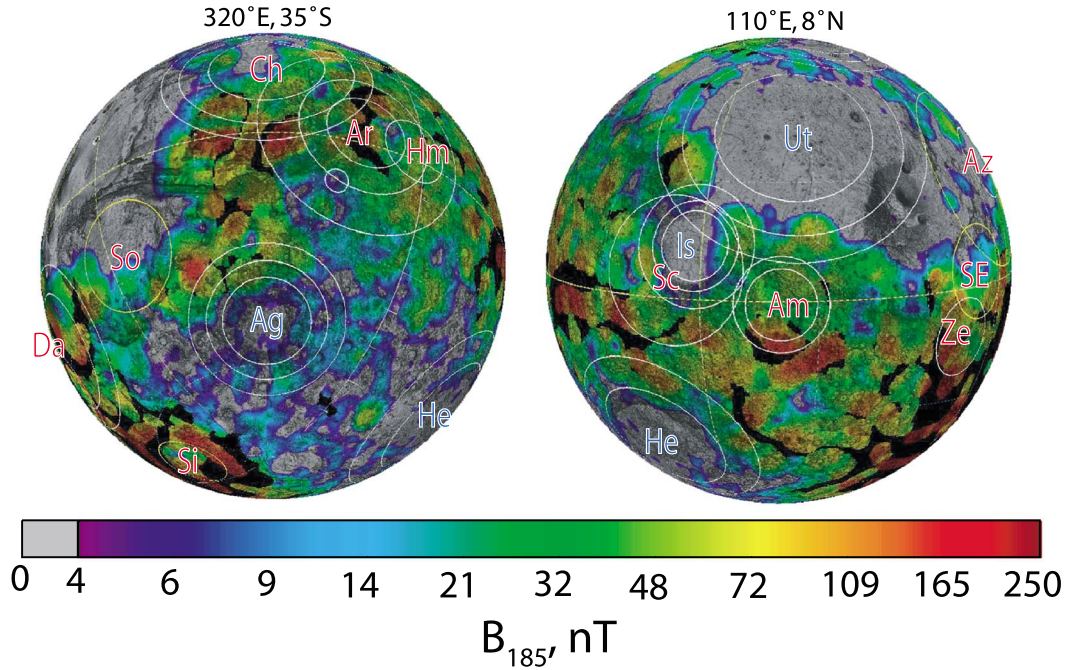


**Figure 1.** Orthographic maps of the crustal magnetic field magnitude at 185 km altitude overlaid on shaded topography [Smith *et al.*, 2001]. The  $B_{185}$  map was adapted from Lillis *et al.* [2008a]. Impact basins  $>1000$  km in diameter are shown as solid circles, where multi-ringed basins have a circle for each ring [Frey, 2008]. Demagnetized and magnetized basins are identified with blue and red lettering, respectively. The letters are abbreviations for the following basins: Daedalia (Da), Solis (So), Chryse (Ch), Ares (Ar), Sireum (Si), Hematite (Hm), Hellas (He), Scopolus (Sc), Isidis (Is), Utopia (Ut), North Polar (NP), Amenthes (Am), Zephyria (Ze), Southeast Elysium (SE), Amazonis (Az).

large, coherently magnetized regions of crust (at least hundreds of kilometers in scale [Acuña *et al.*, 1999, 2001; Connerney *et al.*, 2001], which in turn can only be adequately explained by the past presence of a dynamo-driven global magnetic field comparable in strength to that at the Earth’s surface (i.e.,  $\sim 50$   $\mu$ T).

[5] The very weak crustal magnetic fields measured above the large impact basins Hellas and Argyre have for some time been taken as evidence that the basins were demagnetized by shock and/or thermal effects and hence that the dynamo had likely ceased before the remaining impact-heated crust in the oldest of these basins had cooled below its blocking temperature [e.g., Acuña *et al.*, 1999; Mohit and Arkani-Hamed, 2004]. This hypothesis was strengthened by the more sensitive crustal magnetic field map at 185 km altitude from electron reflection (ER) magnetometry [Mitchell *et al.*, 2007; Lillis *et al.*, 2008a], which also showed that the Utopia, Isidis, and North Polar impact basins (and several more) had similarly very weak magnetic signatures. Crater retention studies revealed these five basins to be the youngest of the large impact basins ( $>1000$  km diameter) [Frey, 2006; 2008], while the 14 oldest basins display substantially stronger magnetic field signatures (Figure 1 shows the magnetic signatures of 5 of the unmagnetized basins and several magnetized basins at 185 km altitude).

[6] This chronology led to the conclusion that a substantial, and possibly rapid, decrease in Martian crustal magnetization occurred around an absolute model age of 4.1 Ga [Lillis *et al.*, 2008b], based on the cratering chronology of Hartmann and Neukum [2001]. We acknowledge other

possible explanations for this rapid, permanent decrease in post-impact magnetization [e.g., Hood *et al.*, 2010]. However, for the purposes of this paper, we will assume the decrease was due to the disappearance of the global magnetic field and that all basins we identify as “demagnetized” formed in the absence of a global field.

### 1.3. Candidate Martian Magnetic Minerals

[7] A key element in understanding how large impacts demagnetize the crust in the absence of an ambient magnetic field is the manner in which magnetic minerals lose magnetization in response to elevated temperatures and pressures. At present, little is confidently known about which minerals may be dominantly responsible for the remarkably strong Martian crustal magnetic field [Acuña *et al.*, 1999]. Section 5 of Dunlop and Arkani-Hamed [2005] provides a review of the candidate minerals: pyrrhotite, titanomagnetite, magnetite, titanohematite, and hematite, in a variety of different domain states, which we briefly summarize below. Lack of sufficient sampling of the Martian crust does not allow us to categorically reject any of these candidates. Single domain (SD) refers to the smallest grain sizes which have a single ferromagnetic domain ( $<0.1$   $\mu$ m in the case of magnetite and  $<100$   $\mu$ m in the case of hematite), pseudo-single domain (PSD) describes intermediate grain sizes, while multidomain (MD) is the largest.

[8] Pyrrhotite occurs in most of the Martian meteorites and is the primary natural remanence carrier in many of them [Rochette *et al.*, 2001]. Pyrrhotite, however, has a low Curie temperature of  $320^{\circ}\text{C}$ , which would concentrate

**Table 1.** Parameters Describing the Best Fits to Equation (1) of the Stepwise Thermal Demagnetization Curves of Pyrrhotite, Magnetite, and Hematite Shown<sup>a</sup>

Best Fit Values	Pyrrhotite	Magnetite	Hematite
$\beta$	0.355	0.211	1.06
$T_{\text{scale}}$	152	7000	20.6
$T_c$	325	580	700

<sup>a</sup>Data and fits are shown in Figure 2.

the crustal magnetism in a shallow thin source layer, and its thermoremanence magnitude is only 40% of magnetite [Dunlop and Arkani-Hamed, 2005]. Both features make it a less appealing candidate compared to other minerals.

[9] Titanomagnetite, describing a range of magnetic minerals with the chemical formula  $[\text{Fe}_3\text{O}_4]_a[\text{Fe}_2\text{TiO}_4]_b$  (where  $a+b=1$ ) is the primary magnetic mineral in fresh terrestrial basalts and in some of the Martian meteorites (e.g., Los Angeles) and while Curie temperatures decrease systematically with increasing  $b$  [Dunlop and Ozdemir, 1997], typical values of  $b=0.6$  give very low Curie temperature of  $150^\circ\text{C}$ . In the heat that would have been present as Martian crust was built up through lava flows or magmatic intrusions [McSween et al., 2003], titanomagnetite indirectly (via titanomaghemite) or directly oxyexsolves to magnetite and ilmenite and is therefore unlikely to be a primary carrier of Mars' current remanent magnetism.

[10] Titanohematite with low Ti content (hemoilmenite) is responsible for some strong terrestrial magnetism when in the form of hematite-ilmenite lamellae [McEnroe et al., 2004]. It has been raised as a candidate for Mars; however, anorthositic crust where titanohematite is favored over magnetite is not very common on Mars [Hargraves et al., 2000].

[11] Hematite is ubiquitous on Mars in the form of surface dust and has been detected in gray crystalline form in Meridiani Planum [Christensen et al., 2000]. Attractively, it has a high Curie temperature of  $670^\circ\text{C}$ , allowing for a thicker magnetic source layer. Both single and multidomain (MD) hematite (with thermoremanence of  $\sim 4\%$  and  $\sim 10\%$  of SD magnetite) [Dunlop and Arkani-Hamed, 2005] can account for the strength of the Martian crustal magnetic fields with crustal concentrations of 1.5 to 3% and 8 to 10%, respectively. Note that these concentrations are much higher than required for SD magnetite to be the dominant magnetic carrier.

[12] Magnetite is the most common magnetic mineral on Earth, has the highest thermoremanence of the candidate minerals, and has been found in several Martian meteorites and spectrally identified in Gusev crater by the Spirit rover [Bertelsen et al., 2004]. Because, unlike hematite, magnetite TRM decreases inversely with grain size above  $0.1\ \mu\text{m}$ , both single domain and pseudo-single domain states (requiring  $\sim 0.3\%$  and  $\sim 3\%$  concentration, respectively, to explain Mars' crustal fields) are possible while multidomain ( $>10\ \mu\text{m}$  is extremely unlikely). Further, it has three accepted genesis pathways on early Mars: oxyexsolution of titanomagnetite (mentioned above), exsolution from iron-bearing silicates including pyroxene [Feinberg et al., 2004], and heat-induced decomposition of siderite precipitated from  $\text{CO}_2$ -rich fluids [Scott and Fuller, 2004]. It is therefore an attractive candidate for Martian crustal magnetism.

#### 1.4. Thermal Demagnetization of Magnetic Minerals

[13] Impact heating and the geothermal gradient necessitate inclusion of the effects of thermal demagnetization in our calculations. The temperature demagnetization response is well known for the aforementioned magnetic minerals, where in zero applied field and as temperature increases, TRM decreases slowly and quasi-linearly at first, then more rapidly as  $T_{\text{Curie}}$  is approached. We choose to represent experimental curves for thermal demagnetization of TRM [e.g., Dunlop, 2009] by an empirical function, a modified version of the cumulative distribution function of the gamma distribution:

$$|M| = \begin{cases} \frac{\gamma(\beta, \frac{T_{\text{Curie}} - T}{T_{\text{scale}}})}{\Gamma(\beta)}, & T < T_{\text{Curie}} \\ 0, & T \geq T_{\text{Curie}} \end{cases} \quad (1)$$

where  $T$  is the temperature in degrees Celsius,  $|M|$  is the normalized remaining magnetic moment,  $\Gamma$  is the gamma function,  $\gamma$  is the lower incomplete gamma function,  $\beta$  is a shape parameter,  $T_{\text{scale}}$  is a scale parameter, and  $T_{\text{Curie}}$  is the Curie temperature at which magnetization drops to zero. As well as temperature, thermal demagnetization of TRM also depends somewhat on grain size of the magnetic mineral, something we cannot know for the Martian crust. However, for grain sizes  $>10\ \mu\text{m}$ , stepwise thermal demagnetization curves for pyrrhotite vary by less than  $\sim 15\%$  [Dekkers, 1989]. Though we do not have comparable stepwise curves for magnetite, available thermal demagnetization curves are similar for different samples of magnetite [see Dunlop, 2009, Figures 4 and 5]. In any case, to reduce the number of free parameters, we choose a single thermal demagnetization curve for each mineral. For pyrrhotite, we use the average of the measured thermal demagnetization curves for all grain sizes between 10 and  $150\ \mu\text{m}$  [Dekkers, 1989]. For magnetite, we use a measured curve for a  $135\ \mu\text{m}$  sample [Dunlop, 2009]. For hematite, we use a measured

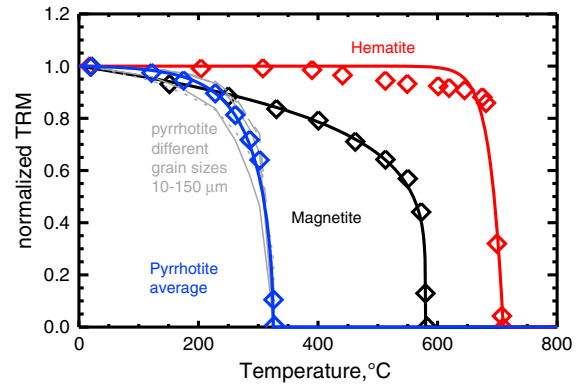


**Figure 2.** Thermal demagnetization curves and fits thereto. Diamonds represent measured stepwise thermal demagnetization curves and solid lines show best fits to equation (1) for pyrrhotite (blue, averaged across grain sizes  $10\text{--}150\ \mu\text{m}$  from Dekkers [1989]), magnetite (black, from Dunlop [2009]), and hematite (red, from Ozdemir and Dunlop [2005]). Light gray lines show separate measured thermal demagnetization curves for the following grain sizes of pyrrhotite:  $10\text{--}15$  (solid line),  $20\text{--}25$  (dotted),  $30\text{--}40$  (dashed),  $55\text{--}75$  (dash-dotted) and  $100\text{--}150$  (dash-dotted-dotted-dotted).

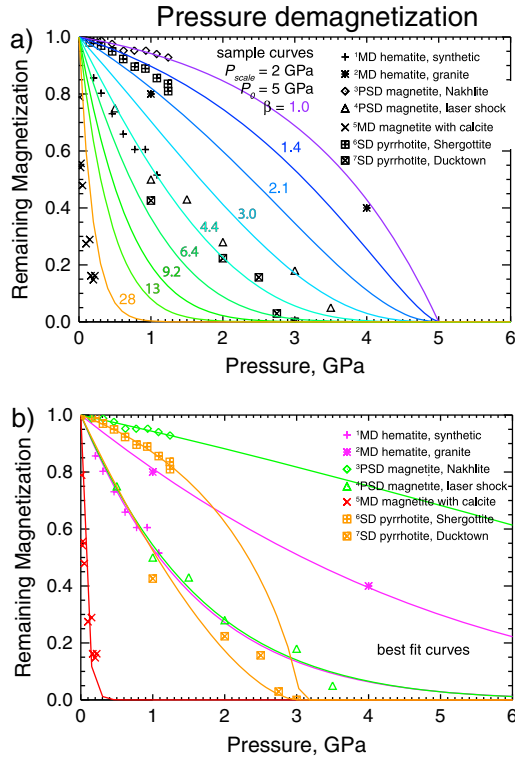


**Figure 3.** Experimental data sets and parameterized curves for pressure-induced decrease of magnetic moment normalized to the initial magnetic moment,  $|M|$ . (a) Experimental data with black symbols and nine curves for  $|M|$  from equation (1) corresponding  $P_{\text{scale}} = 2$  GPa,  $P_0 = 5$  GPa, and  $\beta$  ranging from 1.0 to 28. (b) Measurements are plotted using the same symbols but color coded by magnetic mineral. The solid lines are the best fits to these data, acquired by varying  $\beta$  and  $P_0$  in equation (1) (see Appendix A). References are contained in Table 1.

stepwise thermal demagnetization curve for 0.23  $\mu\text{m}$  grain-size hematite [Ozdemir and Dunlop, 2005]. Table 1 shows the best fit parameters  $\beta$ ,  $T_{\text{scale}}$ , and  $T_{\text{Curie}}$  for each mineral, while Figure 2 shows this thermal demagnetization data and the fits thereto, which we use in this work.

### 1.5. Pressure Demagnetization of Magnetic Minerals

[14] Unfortunately, little experimental data (static or shock) exist for magnetic minerals above  $\sim 1.2$  to 2 GPa, which are pressures insufficient to completely demagnetize most samples. Pressure demagnetization curves for each mineral are dependent on the magnetic domain size, coercivity of the magnetization, and chemistry of the individual minerals [e.g., Rochette et al., 2003; Kletetschka et al., 2004; Gattacceca et al., 2006; Bezaeva et al., 2010; Louzada et al., 2010; Gilder et al., 2006]. Also, materials subjected to hydrostatic, vertical drop, gun shock, and laser shock do not undergo the same loading paths. Furthermore, no terrestrial experiment type can reproduce the strain rates and durations of pressure typical of a natural impact event see [Louzada et al., 2011, Figure 6]. Nonetheless, numerous experiments on the main candidate magnetic minerals on Mars indicate that low pressures of 1–2 GPa result in some significant reduction of magnetization [e.g., Bezaeva et al., 2010;

Louzada et al., 2011]. Identifying mineral specific indicator pressures (e.g., complete demagnetization at a certain pressure) remains difficult at present. Due to this uncertainty, we treat the pressure-demagnetization curve as a free parameter to be investigated (see section 2.1).

### 1.6. Prior Work on Impact Demagnetization at Mars

[15] Much of the previous work on impact demagnetization at Mars has focused on estimating peak pressure contours for specific basins. Hood et al. [2003] first assumed the transient cavity diameters of the Hellas and Argyre basins to be the inner topographic boundary seen today and, with this assumption, used empirical scaling laws derived by Melosh [1989] for (much smaller) craters to estimate radial peak shock pressure contours. More recent work [Mohit and Arkani-Hamed, 2004; Kletetschka et al., 2004; Shahnas and Arkani-Hamed, 2007; Louzada and Stewart, 2009; Arkani-Hamed and Boutin [2012]] obtained much smaller (and different) pressure contours by including a near-surface shockwave interference zone and using different scaling laws and impact parameters. As an example, the 2 GPa pressure contour radius estimates for Hellas have ranged widely, from 1200 km to 3000 km. Arkani-Hamed and Boutin [2012] used the 3 GPa peak pressure contour as a proxy for complete pressure demagnetization. Also, Mohit and Arkani-Hamed [2004] included thermal demagnetization by subtracting the energy lost during decompression from the energy deposited by the shockwave.

[16] These authors then compared these peak pressure (and in the case of Mohit and Arkani-Hamed [2004], temperature) estimates to magnetic field measurements in order to place qualitative constraints on magnetic properties of the crust, acknowledging the aforementioned substantial uncertainty in the location of those contours, the non-unique relationship between magnetization and magnetic field, as well as the paucity of reliable shock demagnetization measurements of the primary candidate magnetic minerals mentioned in the previous section.

### 1.7. Structure and Aims of this Paper

[17] This work aims to avoid scaling laws that are ill-suited to relating large basin topography to impact conditions and instead use hydrocode simulations to account for planetary curvature effects, deformation, melting, and excavation in order to better characterize removal of magnetization by (1) physical displacement, (2) heating, and (3) shock pressure. We also intend to quantitatively include, for the first time, the effects of partial shock pressure and thermal demagnetization.

[18] Section 2 (method) describes our parameterization of pressure-demagnetization curves, a summary of the numerical impact model, specifics of the impact simulations that were conducted, and processing of the simulation results to calculate demagnetization.

[19] Section 3 describes the results of our modeling, where we examine the three demagnetization processes as a function of radius and depth for a single impact energy and mineral and as a function of radius for a few impact energies and several pressure-demagnetization curves, comparing to demagnetization radii of specific Martian basins. Then we examine total demagnetized area as a function of impact energy for the full range of possible pressure-demagnetization

**Table 2.** Details of a Selection of Pressure-Demagnetization Experiments on Candidate Martian Magnetic Minerals<sup>a</sup>

#	Mineral	Sample Description	Experiment Type	Remanence Type	Pressure Range (GPa)	Reference
1	MD hematite	Synthetic	Static	SIRM	0–1.24	<i>Bezaeva et al.</i> [2010]
2	MD hematite	Granite	Gas gun shock	NRM	1–4	<i>Cisowski et al.</i> [1976]
3	PSD magnetite	Martian Nakhlite NWA 998	Static	SIRM	0–1.24	<i>Bezaeva et al.</i> [2007]
4	PSD (titano) magnetite	Basalt, [Fe <sub>3</sub> O <sub>4</sub> ] <sub>0.54</sub> [Fe <sub>2</sub> TiO <sub>4</sub> ] <sub>0.46</sub>	Laser shock	SIRM	0–3.5	<i>Gattacceca et al.</i> [2006]
5	MD magnetite	Natural crushed magnetite with calcite	Static	IRM	0.01–0.22	<i>Borradaile and Jackson</i> [1993]
6	SD pyrrhotite	Basaltic shergottite NWA1068	Static	SIRM	0–1.24	<i>Bezaeva et al.</i> [2007]
7tt	SD pyrrhotite	Pure, Ducktown	Static	SIRM	1–3	<i>Rochette et al.</i> [2003]

<sup>a</sup>SD–single domain; PSD–pseudo-single domain; and MD–multidomain samples. SIRM–saturation isothermal remanent magnetization; IRM–isothermal remanent magnetization; NRM–natural remanent magnetization.

properties, fitting this relationship to an empirical function. Lastly, we calculate, with error bars, the demagnetization area as a function of impact energy for several specific candidate magnetic minerals.

[20] In this paper, we purposely do not categorize impacts by basin size because there does not yet exist any reliable published scaling law for giant basin-forming impacts that relate impact energy to final basin size. In addition, the appropriate diameter of multi-ring basins to use in impact energy scaling relationships is not well established. Instead, we concentrate on the relationship between impact energy and different forms of demagnetization, and how that relationship varies with mineral properties.

## 2. Method

### 2.1. Parameterizing Pressure-Demagnetization Curves of the Crust

[21] We require as simple a parameterization as possible that is consistent with the large range of experimental pressure demagnetization data. For different magnetic minerals and different domain states, the pressure-demagnetization curves range from very concave to quite convex [*Louzada et al.*, 2011]. The simplest function we found that can accommodate this behavior is the same function we used to represent thermal demagnetization, i.e. a modified version of the cumulative distribution function of the gamma distribution:

$$|M| = \begin{cases} \frac{\gamma(\beta, \frac{P_0 - P}{P_{\text{scale}}})}{\Gamma(\beta)}, & P < P_0 \\ 0, & P \geq P_0 \end{cases} \quad (2)$$

where  $P$  is the applied pressure,  $|M|$  is the normalized remaining magnetic moment,  $\Gamma$  is the gamma function,  $\gamma$  is the lower incomplete gamma function,  $\beta$  is a shape parameter,  $P_{\text{scale}}$  is a scale parameter, and  $P_0$  is the pressure at which magnetization drops to zero. Varying  $P_{\text{scale}}$  or  $\beta$  generally mimic each other, so we need not separately vary  $P_{\text{scale}}$ . Figure 3 shows examples of curves defined by equation (1), as well as eight example data sets from pressure-demagnetization experiments. The best fits, according to equation (1), are color coded by magnetic mineral and assume  $P_{\text{scale}} = 2$ . As shown in Figure 3, larger values of  $\beta$  correspond to more concave pressure-demagnetization relationships. Table 1 describes the measurements and provides references. Best fit values of the parameters  $\beta$  and  $P_0$  are not provided in Table 2 because the incompleteness of the demagnetization causes the  $\chi^2$  surface not to have a narrow, well-defined minimum, i.e., the parameters are not

orthogonal within the pressure ranges of the experiments. Detailed plots showing the fits are contained in Appendix A.

[22] This set of seven pressure-demagnetization curves is not intended to be exhaustive (a comprehensive list is compiled by *Louzada et al.* [2011]), but is intended to demonstrate (a) the wide variety of pressure-demagnetization characteristics across all candidate minerals and for different samples of the same mineral and (b) the utility of equation (1).

### 2.2. The Numerical Impact Model

[23] In this work, we use the CTH shock physics code to model basin-scale impact events on early Mars. CTH is a multidimensional and multimaterial finite volume Eulerian shock physics code with second order accuracy [*McGlaun et al.* 1990] that is widely used in planetary impact studies, including comparisons with laboratory craters [*Senft and Stewart*, 2007; *Pierazzo et al.*, 2008], impact basins [*Schultz and Crawford*, 2008; *Stewart*, 2011; *Stewart*, 2012; *Wieczorek et al.*, 2012], and the moon-forming impact [*Canup and Barr*, 2010; *Crawford*, 2010; *Crawford and Kipp*, 2010]. CTH is able to calculate self-gravity in 3-D [*Crawford*, 2010] using the *Barnes and Hut* [1986] algorithm, which is similar to self-gravity implementations in other hydrocodes [e.g., *Canup and Asphaug*, 2001; *Springel*, 2005]. The current simulations use a fixed central gravity field for 2-D calculations of basin-sized impacts on spherical planets (see Figure 3) in order to allow for greater spatial resolution of the crust than possible with 3-D simulations.

[24] The CTH code has recently been updated to include more realistic rock rheology under high strain-rate conditions [*Senft and Stewart* 2007, 2009; *Zucker and Stewart* 2010; *Stewart* 2011]. The latest improvements in the code include more realistic treatments of thermal weakening as the solidus is approached for mantle materials [e.g., *Zhang and Herzberg* 1994]. In addition to the use of massless Lagrangian tracer particles to provide time histories of discrete parcels of material, extra variables have been added to record the original positions and peak shock pressures and temperatures of all material as it is advected through the mesh. For similar rheological models and equations of state, the transient and final basin sizes are similar to calculations using comparable shock physics codes (e.g., *iSALE* [*Ivanov et al.* 2010]). High-resolution simulations of basin-sized impacts have strong agreement with observations of terrestrial [*Senft and Stewart* 2009] and extra-terrestrial [*Stewart*, 2012, *Wieczorek et al.* 2012] impact basins, including mantle uplift and the locations of major faults.

[25] It remains difficult to relate topographic features present just hours after the simulated impact with present-

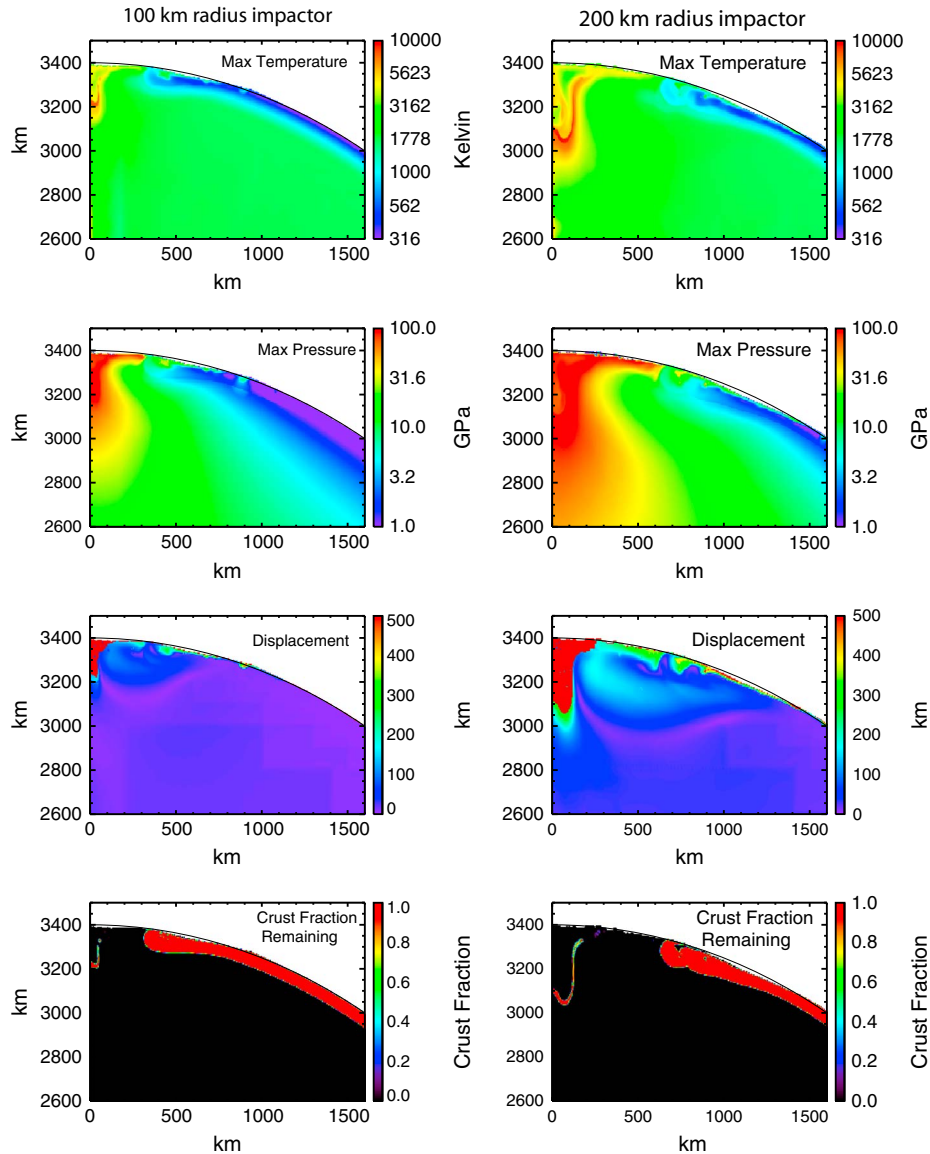


**Figure 4.** Curvature effects in 2-D impact simulations. Maximum temperature, maximum pressure, displacement, and fraction of original crust are plotted for two different impactor radii: 100 km (left column) and 200 km (right column). The impact velocity was 10.6 km/s.

day features of giant basins such as the basin floor, various scarps, and sometimes multiple rings (e.g., for Argyre) [Stewart, 2012], owing to processes that occur on much longer time scales. Consequently, it remains difficult to relate a specific large impact basin on Mars to a single impact energy, in contrast to smaller craters with simple topographies, for which crater scaling laws are well established [e.g., Melosh, 1989]. In order to avoid further substantial uncertainty, in this paper we will limit the investigation to impact energies and not discuss the final topographic radii of basins.

### 2.3. Impact Model Parameters

[26] Since the large (>1000 km diameter) Martian basins date from ~4 Ga, for the initial thermal state of the planet we are guided by the crustal evolution calculations of Hauck and Phillips [2002]. Their nominal model, which produces

about 50 km of crust over 4.5 Gyr, provides an upper limit to the thermal gradient because the majority of the Martian crust must have formed within the first 100 Myr [Nimmo and Tanaka, 2005]. For this work, we assume a surface temperature of 298 K and a thermal gradient consistent with a heat flow of 60 mW/m<sup>2</sup>, reasonable for the middle Noachian, and a pre-impact crust of 50 km thickness [Neumann et al., 2004; 2008]. We use tabulated multiphase equations of state for the core (iron) [Kerley, 1993], mantle (dunite) [Benz et al., 1989]), and crust (silica [Melosh, 2007]), with an impactor also composed of dunite. The planet is initialized in lithostatic equilibrium with a density of the crust of 2.65 g cm<sup>-3</sup> and a density at the top of the mantle and in the projectile of 3.32 g cm<sup>-3</sup>.

[27] The rheological parameters for the crust and mantle are based on laboratory experiments at the appropriate strain rates [Senft and Stewart 2009; Zucker and Stewart 2010; Stewart

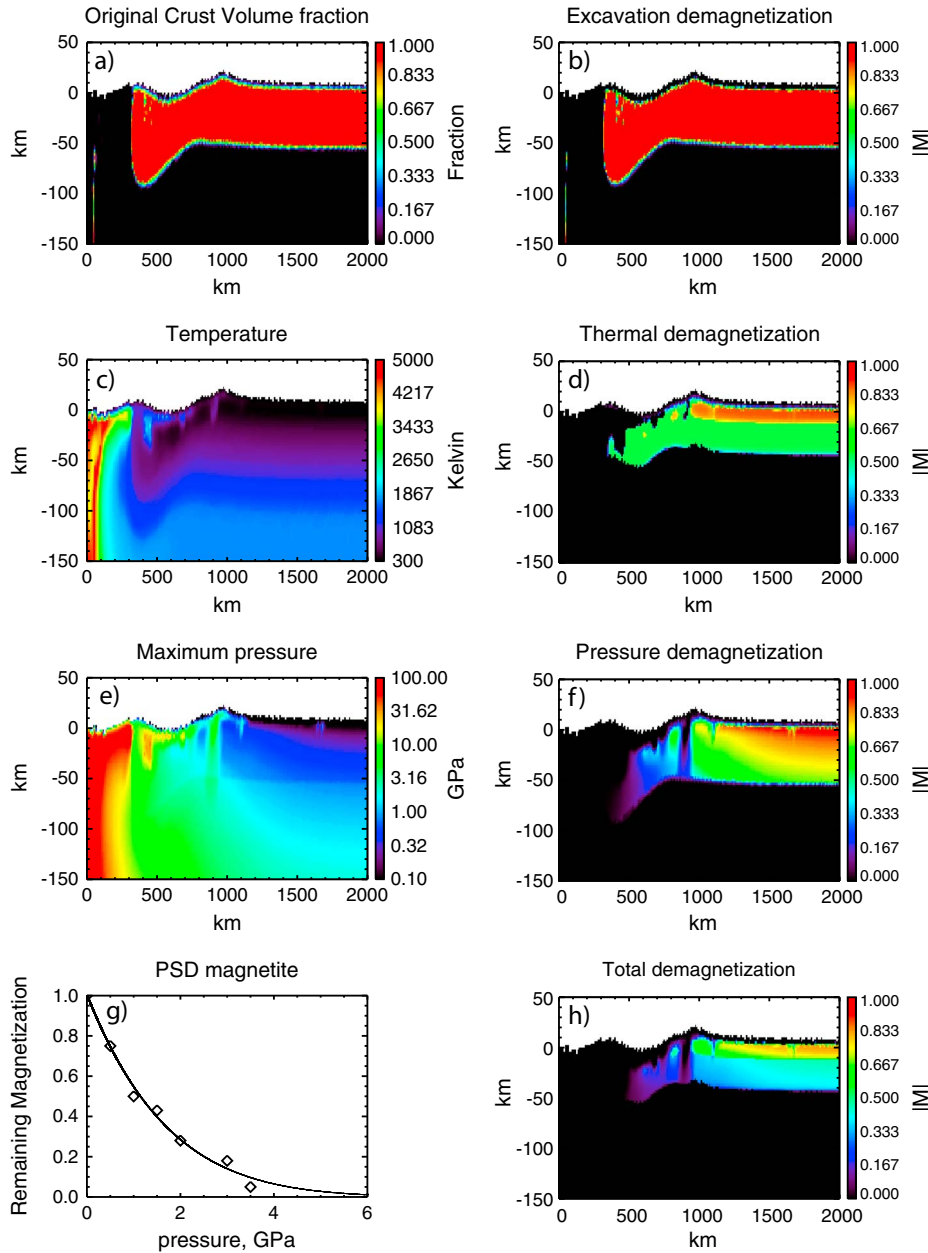


**Figure 5.** Simulated physical quantities and resulting normalized magnetization following the impact of a 100 km radius dunite bolide on the surface of Noachian Mars at 15 km/s and a 45° angle. (a) The volume fraction of original crust and (b) the resulting remaining magnetization. (c, d) The maximum temperature reached and the resulting thermal demagnetization calculated using equation 1 and the magnetite values from Table 1. (e, f) The maximum pressure reached and the resulting shock demagnetization. (g) The assumed pressure-demagnetization curve used for calculating the demagnetization in panel (f) as a best fit to the experimental shock demagnetization data from *Gattacceca et al.* [2006] for pseudo-single domain (PSD) magnetite. (h) The total remaining magnetization from the combined effects of excavation, heating, and pressure.

2011]. Previous work indicates that the final crater size does not vary significantly for the observed range of rheological parameters for a given rock type [Senft and Stewart 2009]. Crustal flow back into the crater is at present artificially inhibited in all numerical impact models [Stewart 2012]; as a result, the final basins have an incorrect central zone with a complete lack of crust. In addition, the latent heat of melting is not included in the equation of state models, so the final

temperatures in the melt sheet are artificially elevated. We do not expect either shortcoming to significantly affect final temperatures or peak pressures outside the transient cavity where partial demagnetization begins (see section 3).

[28] In this work we shall consider an ensemble of runs, performed for vertical impactor velocities of 10.6 km/s (corresponding to the vertical component of a 45° impact at 15 km/s) and impactor radii of 15, 25, 50, 100, 150,

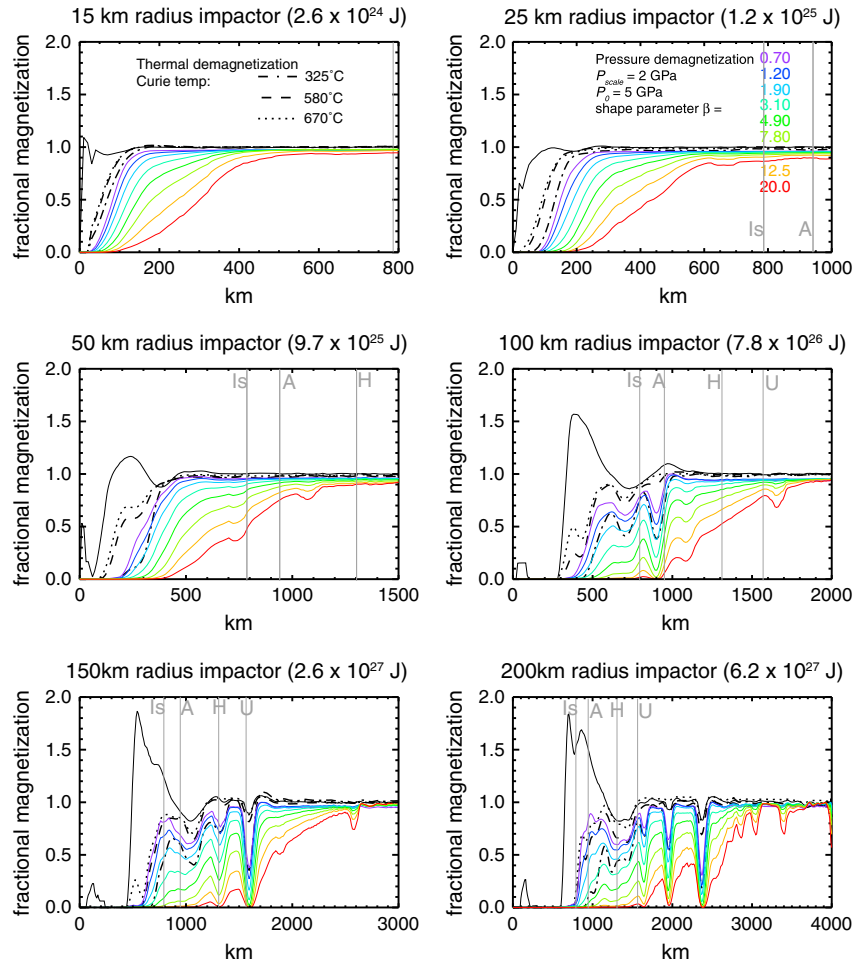


**Figure 6.** Curves are plotted for excavation, thermal, and shock pressure demagnetization as a function of radius from the impact point. Dash-dotted, dashed, and dotted black lines represent thermal demagnetization for Curie temperatures of 325°C (pyrrhotite), 580°C (magnetite), and 670°C (hematite). Colored lines represent shock demagnetization for pressure-demagnetization curves (as defined by equation (1)) with  $P_{scale} = 2$  GPa,  $P_0 = 5$  GPa, and shape parameter  $\beta$  ranging from 0.75 to 20. The light gray vertical lines represent demagnetization radii for four of the large ancient impact basins on Mars: Isidis (Is), Argyre (A), Hellas (H), and Utopia (U) as determined by *Lillis et al.* [2010].

200, and 250 km. The simulations utilized the adaptive mesh refinement feature in CTH, which allows the material of interest to remain gridded to a specified resolution. In the impacted hemisphere, the spatial resolution in the crust was 2.5 km/cell. During the initial stages of crater formation, the projectile was resolved at 1.25 km/cell for the 15 and 25 km radii cases. The resolution in the mantle varied from 2.5 to 10 km/cell with increasing projectile size.

[29] We conducted the 100 km, 150 km, and 200 km impactor radius cases separately at 2.5 km/cell and 5 km/cell and found no statistical difference in radial demagnetization profiles. We concluded that using 2.5 km/cell in the crust constitutes adequate resolution.

#### 2.4. Processing of Impact Modeling Results

[30] The impact model output includes the following properties for each parcel of material in the mesh:

[31] 1. Initial and final location,

[32] 2. Final volume fractions of impactor, crust and mantle,

[33] 3. Maximum pressure occurring in impactor, crust and mantle fractions, and

[34] 4. Final temperature.

[35] As the simulations runs had different initial grids, the material information was interpolated to a regular Cartesian grid. To illustrate this process, Figure 4 shows two-dimensional plots of maximum temperature, maximum pressure, displacement (i.e., distance traveled by the tracer during impact event), and the crustal fraction remaining at 8000 s after impact, for two different impactor radii: 100 km and 200 km.

[36] Recall our assumption that no ambient field is present as the post-impact materials cool through their magnetic blocking temperature. Therefore, in examining the remaining magnetization, we are interested only in material that was considered crustal before the impact (and therefore possibly magnetic), since “new” crust derived from impactor or mantle material would be unmagnetized in this scenario (i.e., even if it

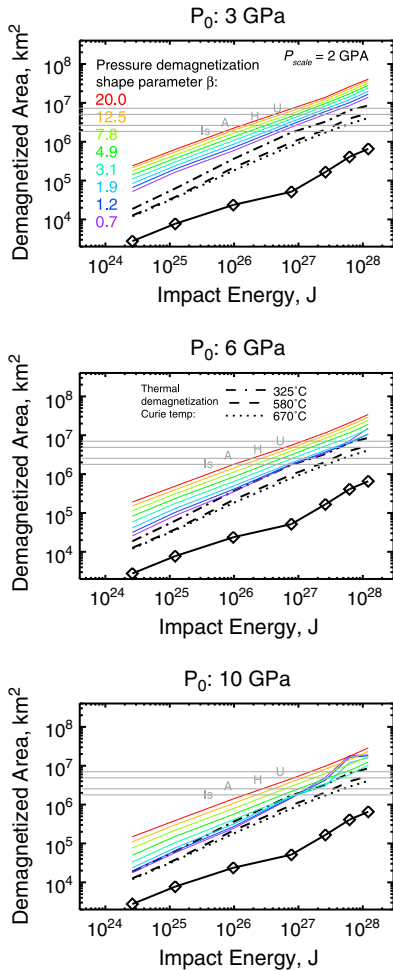


**Figure 7.** Demagnetized area from excavation, thermal effects, and shock pressure are plotted as a function of impact energy. The solid black line and diamonds represent excavation. Dash-dotted, dashed, and dotted black lines represent thermal demagnetization for Curie temperatures of 325°C (pyrrhotite), 580°C (magnetite), and 670°C (hematite). Colored lines represent shock demagnetization for pressure-demagnetization curves (as defined by equation (1)) with  $P_{\text{scale}} = 2$  GPa and shape parameter  $\beta$  ranging from 0.75 to 20, with  $P_0 = 3, 6, 10$  GPa in the top, middle, and bottom panels respectively. The light gray horizontal lines represent demagnetization areas for four of the large ancient impact basins on Mars: Isidis (Is), Argyre (A), Hellas (H), and Utopia (U) as determined by *Lillis et al.* [2010].

were ferromagnetic material). This material is in a relatively thin layer ( $< 100$  km) at the surface. For the purposes of examining this depth of interest, which is small compared with the radius of Mars and the size of both the final topographic basin and the demagnetized diameter (both  $> 1000$  km) [*Lillis et al.*, 2010], we choose to reproject the outer layer of the planet and further interpolate all relevant quantities (e.g., pressure, temperature, magnetization, etc.) to a two-dimensional half-space defined by depth from the original surface and radius from the impact point. We use this coordinate system hereafter in this paper for the purposes of examining the relative importance of shock, thermal, and excavation for demagnetization in giant impacts.

## 2.5. Post-Impact Thermal Evolution

[37] Since the impact modeling simulates only the dynamic phase after the impact and covers at most a few hours of simulated time, we must calculate the subsequent thermal evolution of the half-space. We assume that heat transfer within Mars occurs by conduction alone, use the temperature-dependent thermal conductivity of *Whittington et al.* [2009]. The surface temperature quickly equilibrates to the pre-impact surface temperature assumed in the simulations (298°K). We simulate 30 Ma of thermal evolution as longer times have minimal effect on the peak temperatures. We then recorded the maximum temperature reached at all points in the simulation space, which is the key metric for thermal demagnetization.

[38] Hydrothermal activity may have the ability to somewhat further alter temperatures, but *Ogawa and Manga* [2007] demonstrated that such activity has a negligible effect on magnetization for permeabilities less than  $10^{-15}$  m<sup>2</sup>, i.e., below at most a few km depth [*Saar and Manga*, 2004]. We thus ignore any possible hydrothermal effects on maximum temperatures.

## 3. Results

### 3.1. Case Study of Demagnetizing Processes: Excavation, Shock, and Heating

[39] As stated earlier, demagnetization in large impacts occurs via shock, heating, and excavation of magnetized pre-impact crust. Before investigating in detail the dependencies of these three kinds of demagnetization on impact energy and mineral properties, it is useful to examine a single example in some detail in order to better understand the relationship between the impact process and resulting demagnetization. We take as a representative case, a 100 km radius bolide impacting at 10.6 km/s, with a kinetic energy of  $7.7 \times 10^{26}$  J (equivalent to 217 billion megatons of explosive). Figure 5 shows the depth and radial extent of excavation, heating, and shock, as well as the resulting demagnetization for a pseudo-single domain (PSD) magnetite/titanomagnetite mixture ( $[\text{Fe}_3\text{O}_4]_{0.54}[\text{Fe}_2\text{TiO}_4]_{0.46}$ ) from a terrestrial basalt sample [*Gattacceca et al.*, 2006].

[40] The numerical methods of impact models do not include long-term topographic relaxation processes and lack the rheological details and spatial resolution necessary to robustly capture the topographic relief a few hours after impact. In these simulations, the inner “ring” is 8–10 km higher than the center of the basin, while the outer (plausibly the main) “rim” is  $\sim 20$  km higher, approximately twice what we see today for large Martian basins such as Hellas and Argyre [*Smith et al.*, 2001]. If we assume that the “ridge” at  $\sim 350$  km will relax, that the resulting flat basin “floor” will extend out to 650 km, and that the main rim is around 950 km, we could say that this impact is “Hellas-like,” but as mentioned in section 2.4, we do not make any such assumptions as part of the analysis in this paper and we will not attempt to associate a single impact energy with a final basin size or any specific basin on Mars.

[41] The excavated portion of the basin is physically removed during the process of crater formation. Some of this material will exceed the escape velocity of 5 km/s (forming the source of Martian meteorites on Earth). As well as being

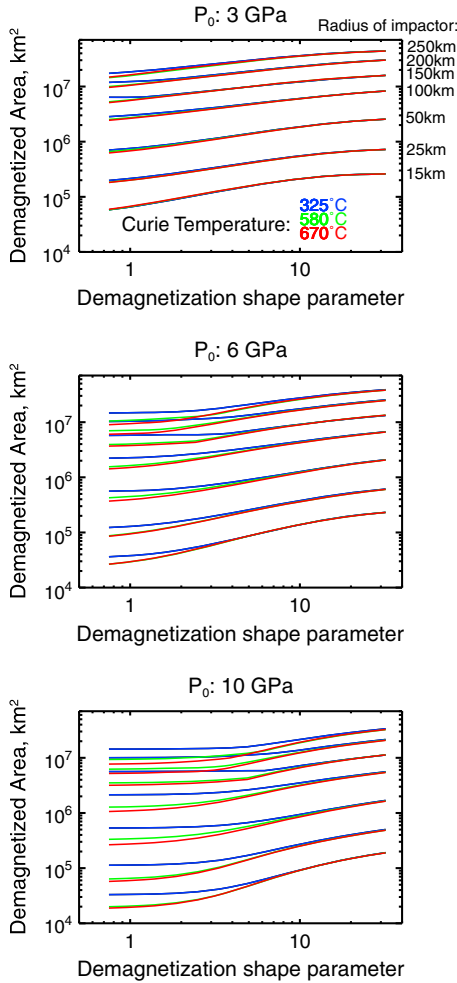


**Figure 8.** Total demagnetized area (equation (3)) as a function of demagnetization shape parameter  $\beta$ . Blue, green, and red lines represent Curie temperatures of 325°C (pyrrhotite), 580°C (magnetite), and 670°C (hematite) respectively, while each family of curves represent a single impact energy and each panel shows a different value of  $P_0$ .

shocked and heated, the remaining material which re-impacts Mars is also mixed, reoriented, and scattered over the surrounding area in an ejecta blanket. Any significant pre-impact magnetic coherence can be expected to be destroyed by such excavation and redistribution, so we do not include any contribution to magnetization from this material and, as mentioned earlier, we do not assume any of the new crust inside the basin can be magnetized. The distribution of “excavation demagnetization” is shown in Figures 5a and 5b.

[42] The spatial distribution of the maximum temperature is shown in Figure 5c, while the resulting thermal demagnetization, calculated with the appropriate fractions ( $T_{\text{Curie}} = 150^\circ\text{C}$  for 46% titanomagnetite,  $T_{\text{Curie}} = 580^\circ\text{C}$  for 54% magnetite), is shown next to it in Figure 5d. Note that we assume that the pre-impact geothermal gradient will reassert itself after a sufficient time and therefore demagnetize all parcels of material deeper than the Curie isotherm at the (relatively undisturbed) edge of the simulation domain. This can be seen in the left-to-right downward slope of the base of the magnetized crust in Figure 5d. We found that including the post-

impact thermal evolution calculation made a substantial difference to total demagnetization only in the case of pyrrhotite (325°C Curie temperature), while the difference was small to negligible in the cases of the higher Curie temperature minerals magnetite and hematite.

[43] In the innermost regions of the basin, we see a superheated plug of mantle material (which has been uplifted by crater collapse processes) and a rapid decay of temperature with distance toward the crater rim. We see substantial near-surface demagnetization out to  $\sim 600$  km. There are a few shock-heated “tendrils” of higher temperature extending from the surface to depths that decrease with radius, caused by larger clumps of re-impacting ejecta.

[44] Figure 5e shows the maximum pressure reached. We see the classical pseudo-isobaric core extending out to 250–300 km, followed by an approximately exponential decay with radius, interrupted by the aforementioned “fingers” of shock from re-impacting ejecta. We then calculate the resulting distribution of remaining magnetization (Figure 5f), assuming the best fit of equation (1) to the pressure-demagnetization data from PSD (titano-)magnetite sample from *Gattacceca et al. [2006]* (shown in Figure 5g). In this case, while complete pressure demagnetization does not occur outside the transient cavity except at shallow depth, the effects of shock pressure extend past 1500 km.

[45] The net result of these three effects, i.e., the total demagnetization, is shown in Figure 5h. We calculate total demagnetization by multiplying these three effects, a valid approach because the excavation demagnetization is treated as a binary process and because shock and thermal demagnetization will not occur at exactly the same time. Comparing the panels in the right-hand column of Figure 5, we see that for this (fairly typical) case of a giant impact into crust whose primary magnetic carrier is PSD (titano-) magnetite, the relative effects of our 3-D demagnetizing processes can be summarized as (1) prior crust is completely excavated within the transient cavity out to 325–350 km, (2) sufficient heat is generated outside the transient cavity to completely demagnetize a substantial volume of rock, extending out to  $\sim 450$  km and to partially demagnetize out to  $\sim 1000$  km, and (3) shock demagnetization of at least 50% extends out to  $\sim 900$  km, with substantial uncertainty in the demagnetization fraction inside that radius due to incomplete pressure demagnetization data in the literature. Note that crust that collapses into the crater is mixed with the melt sheet and would not impart a coherent magnetic signal.

### 3.2. Comparing Thermal Versus Shock Demagnetization: 1-D Profiles

[46] We now conduct a systematic investigation into the relative and absolute effects of thermal versus shock demagnetization as a function of impact energy and mineral properties. For example, we would like to observe how the demagnetization patterns changes with the Curie temperature and the shape and zero-value parameters  $\beta$  and  $P_0$  in equation (1). We would also like to know whether there could be plausible cases where thermal effects outweigh shock effects.

[47] In our example case, we looked at the full two-dimensional detail. However, to make investigation of several parameters practical, we first eliminate one of the dimensions, namely, depth. This is because changes in demagnetization with depth are much more difficult to

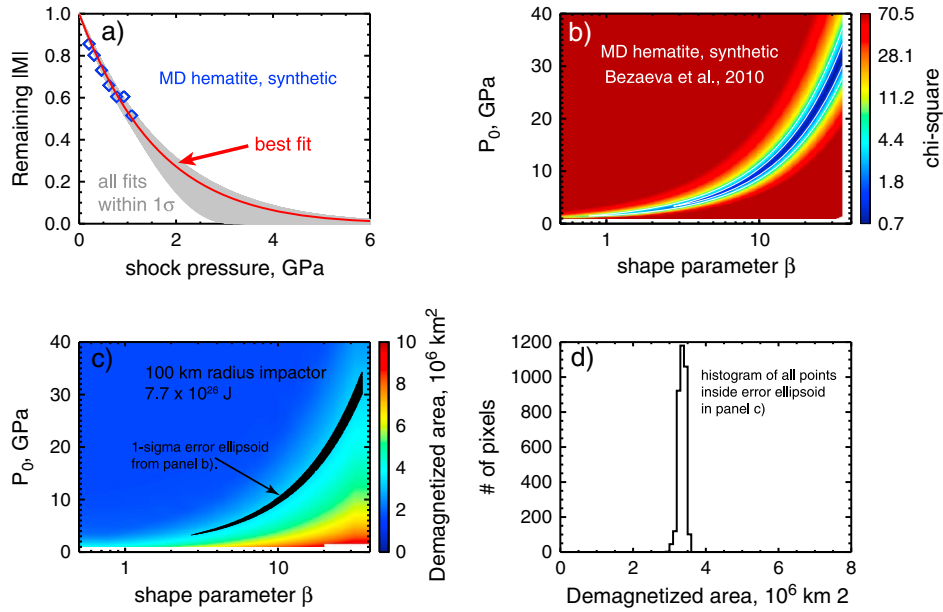


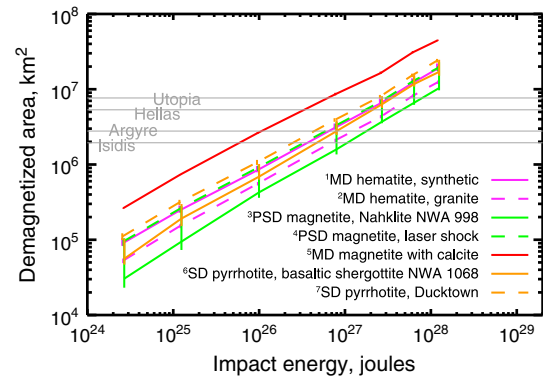
**Figure 9.** Determining the possible range of demagnetized area for a single pressure-demagnetization data set. (a) The data points are in blue (with a typical error of approximately  $\pm 0.03$ ). The red line shows the best fit, while the gray lines represent all plausible fits within the 1-sigma error ellipsoid. (b) The  $\chi^2$  surface for the fits, with white contour lines at minimum  $(\chi^2) + 0.5$  and minimum  $(\chi^2) + 1.0$ . (c) The demagnetized area for the 100 km radius impactor case, as a function of  $\beta$  and  $P_0$ , with the same error ellipsoid shown in black. (d) A histogram of all of the values of demagnetized area within the error ellipsoid for this case.

observe in orbital magnetic field data than changes with respect to radius. For every radial value, we sum the magnetization in the vertical column and divide by the sum of pre-impact magnetization in the same column. We do this separately for excavation, thermal, and shock demagnetization. Figure 6 shows demagnetization as a function of radius from the impact point, separately showing physical removal, thermal demagnetization (for the Curie temperatures of pyrrhotite, magnetite, and hematite), and shock demagnetization (for a reasonable fixed value of  $P_0 = 5$  GPa) and a range of  $\beta$  values from 0.75 (convex) to 20 (concave), i.e., the same family of curves as shown in Figure 3a, for six impactor radii spanning 15–200 km.

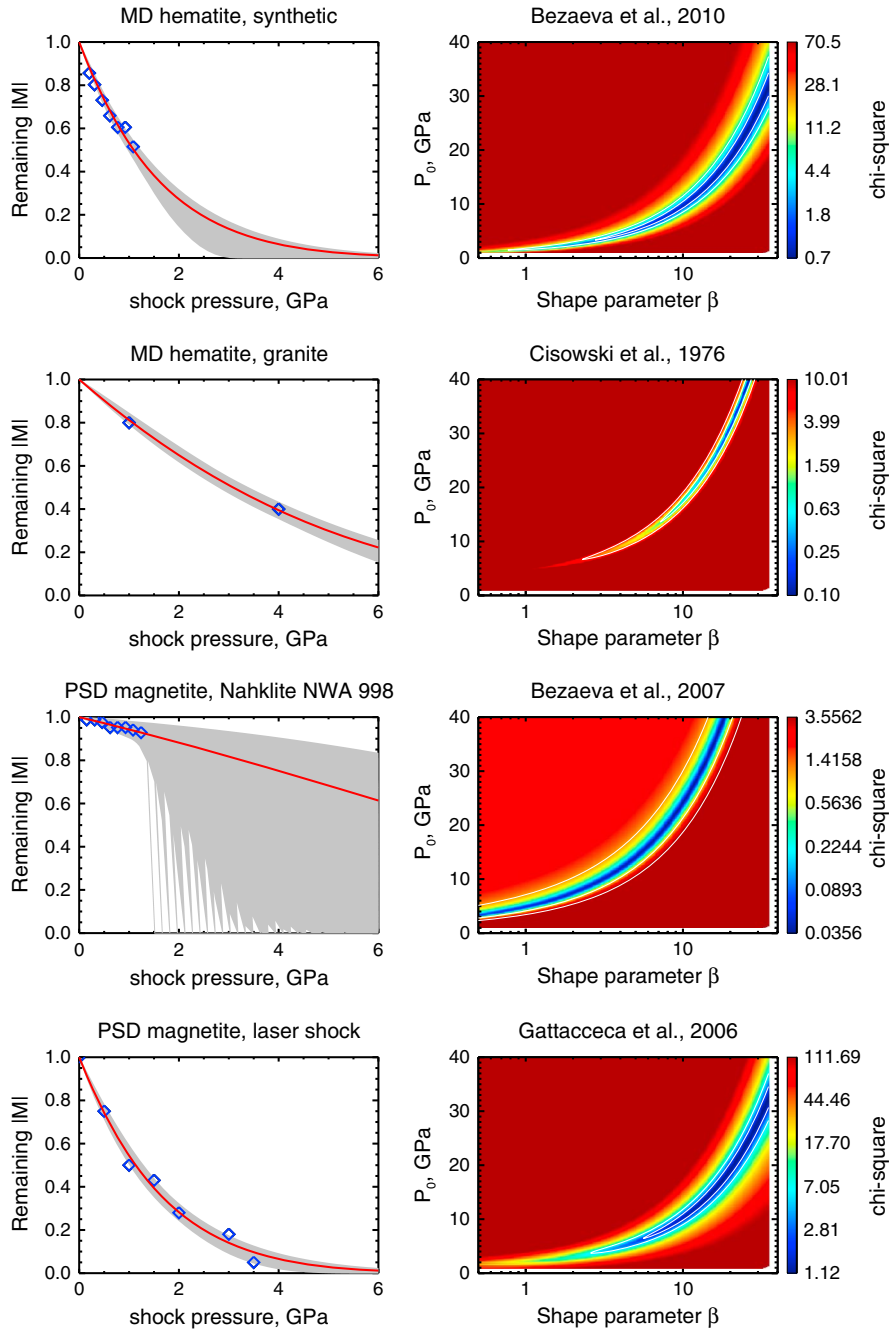
[48] We see that for the smaller impacts (15 and 25 km radius impactor), shock pressure dominates over thermal effects for our three plausible Curie temperatures, and excavation is almost negligible by comparison. However, as impact size increases and more plastic deformation occurs, we start to see a non-negligible overlap between shock and thermal demagnetization. One mineral for which this may be true is single domain pyrrhotite (see Figure 2), where a  $\beta$  value of less than  $\sim 4$  and a Curie temperature of  $325^\circ$  Celsius could lead to more thermal than shock demagnetization around 325 km from the impact point for the 50 km impactor and 500 km from the impact point for the 100 km impactor.

[49] Figure 6 also shows the best fit radii of demagnetization for four of the largest ancient Martian impact basins Isidis, Argyre, Hellas, and Utopia, as determined by *Lillis et al.* [2010] using multiple altitude magnetic field data and a Monte Carlo/Fourier representation of magnetization. In that work, the radius of demagnetization was defined as the middle of a “ramp-up” zone at the edge where the normalized magnetization increased linearly from 0 to 1. While

the width of the ramp-up zone was poorly constrained by data, the demagnetization radii were constrained (within the confines of the model used) to an accuracy of 10–20%. Thus, it is instructive to compare those data-derived demagnetization radii with the predicted demagnetization-versus-radius curves in order to examine qualitatively which



**Figure 10.** Demagnetized area is plotted as a function of impact energy for the same seven magnetic minerals shown in Figure 2. Each color represents a different mineral: pink-MD hematite, green-PSD magnetite, and orange-pyrrhotite. Vertical error bars represent the maximum and minimum values of demagnetized area within the 1-sigma error ellipsoid of fits to equation (1) (e.g., the distribution shown in Figure 9d). The light gray horizontal lines represent demagnetization areas for four of the large ancient impact basins on Mars: Isidis (Is), Argyre (A), Hellas (H), and Utopia (U) as determined by *Lillis et al.* [2010].

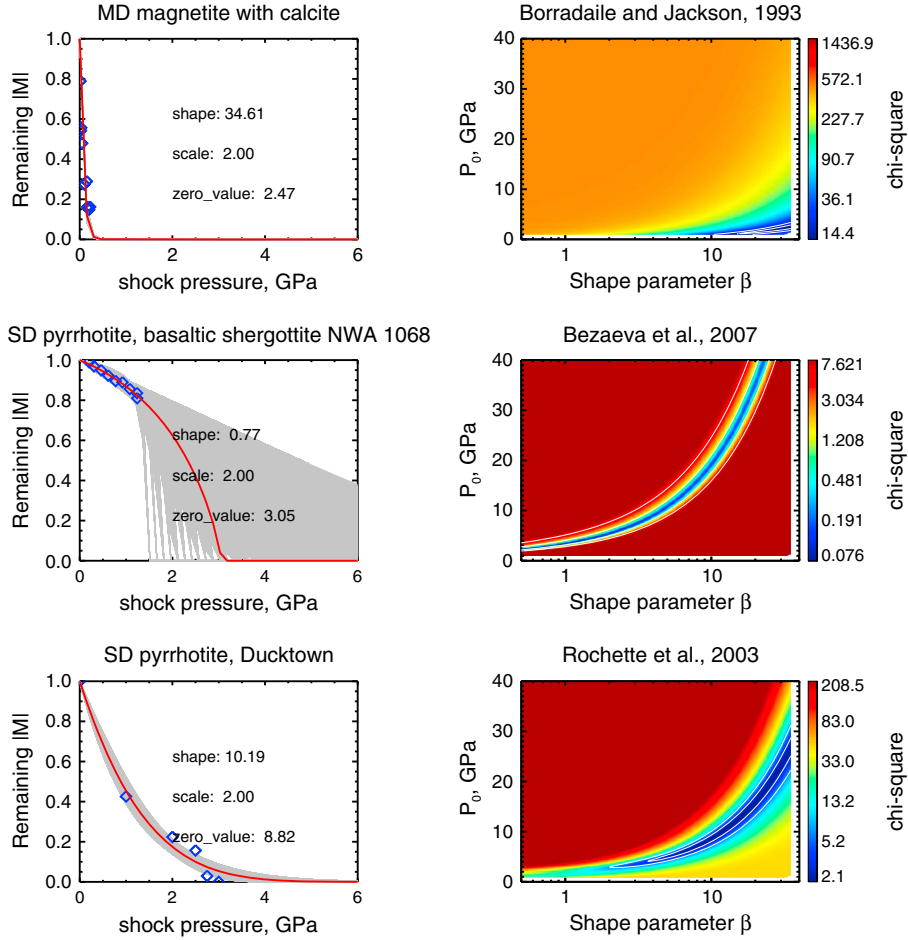


**Figure A1.** Fit details for pressure-demagnetization of candidate Martian magnetic minerals. Each row represents a single experimental data set. The left column shows the data points in blue (with a typical error of approximately  $\pm 0.03$ ). The red line shows the best fit, while the gray lines represent all plausible fits within the 1-sigma error ellipsoid. The right column shows the  $\chi^2$  surface for the fits, with white contour lines at minimum ( $\chi^2$ ) + 0.5 and minimum ( $\chi^2$ ) + 1.0.

combinations of impact energies and mineral property are consistent with each basin.

[50] For example, the demagnetization radius of the Isidis impact is consistent with an impact energy of  $\sim 4 \times 10^{26}$  J if the magnetic mineral has a high  $\beta$  value (i.e., is easily demagnetized like multidomain magnetite) [Borradaile and Jackson, 1993], whereas it would require  $\sim 10$  times more energy if the mineral has a much lower value of  $\beta$ , i.e., more difficult to demagnetize, like pseudo-single domain magnetite [Bezaeva et al., 2007]. To explain the demagnetization

at Hellas or Utopia, the multiple large re-impacting ejecta fragments make interpretation more difficult. Discontinuities in the ejecta curtain could cause spatially heterogeneous signatures of demagnetization outside the primary central demagnetized area, but if the simulations are indeed realistic, the ejecta fragments created demagnetized zones only  $\sim 100$  km wide, small enough to be “smoothed out” in orbital magnetic field data. Utopia would then be consistent with an impact energy of  $\sim 4 \times 10^{27}$  J and a  $\beta$  value of 20. If  $\beta \sim 1$ , then a huge impact of several times  $10^{28}$  J (or a


**Figure A1.** (continued)

colossal bolide, or planetesimal  $>350$  km in radius) would be required.

### 3.3. Demagnetized Area

[51] We have examined impact demagnetization in two dimensions (radius and depth; section 3.1) and one dimension (just radius; section 3.2). In the first instance, we considered only a single impact energy, Curie temperature, and pressure-demagnetization curve. In the second instance, though we explored several impact energies and values of  $\beta$ , we were limited to a single value of  $P_0$ . In order to obtain an overview of the effects of all relevant parameters on impact demagnetization, we find it useful to define the total demagnetized area  $A$  for a given set of impact and mineral parameters.

$$A = 2\pi \int_0^R (1 - |M(r)|r)dr \quad (3)$$

where  $|M(r)|$  is normalized magnetization as a function of radius and where we assume azimuthal symmetry. Figure 7 plots the area demagnetized by excavation, thermal, and shock pressure effects for a range of reasonable values of Curie temperature and the shock pressure parameters  $\beta$  and  $P_0$ , with the same color/line legend as Figure 6, but with

the radius dimension collapsed. Figure 8 shows the same information as Figure 7, but shows only total demagnetized area (i.e., not separated by process) and plots demagnetized area as a function of shape parameter, with different curves for each impact energy and Curie temperature.

[52] First we notice the demagnetized area  $A$  has a power law dependence on impact energy. While the excavated area has a break in the power law around  $10^{27}$  J, the thermally demagnetized and shock demagnetized areas have a single power law exponent ranging from 0.60 to 0.75. We notice again that thermal demagnetization is only possibly important for pyrrhotite, never for magnetite or hematite. In the case of pyrrhotite, we observe that thermal demagnetization is relatively unimportant for combinations of lower impact energies, larger values of  $\beta$  and smaller values of  $P_0$  and becomes increasingly important as impact energies and  $P_0$  increase and as  $\beta$  decreases. Although all three parameters individually affect demagnetized area, it is generally the case that for values of  $P_0$  of 6 GPa and higher, values of  $\beta$  of  $\sim 5$  and lower, and for impact energies above  $10^{27}$  J, a larger total volume of pre-impact crust is effectively raised above the Curie temperature of pyrrhotite than is shock demagnetized.

[53] As also discussed in the previous section, a single value of demagnetized area (such as those calculated by

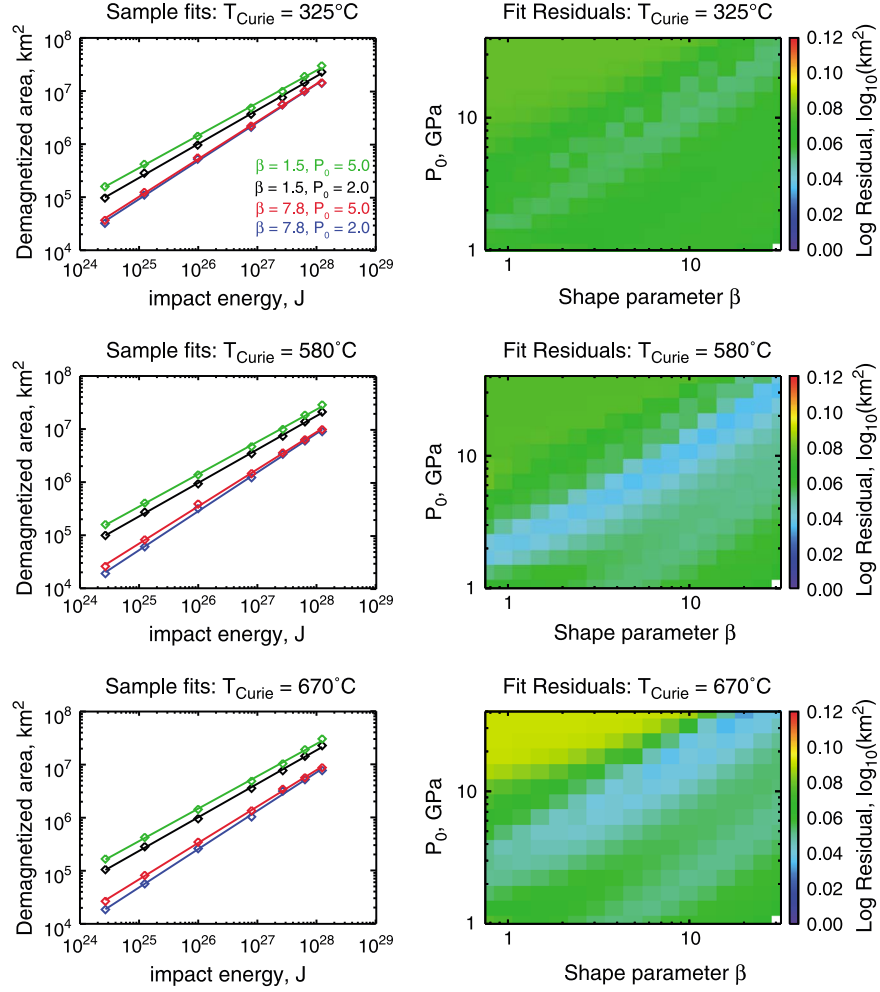


**Figure B1.** Power law fits to demagnetized area as a function of impact energy. The top, middle, and bottom rows are for Curie temperatures of 325°C (pyrrhotite), 580°C (magnetite), and 670°C (hematite), respectively. The left column shows four sample fits. The diamonds are the demagnetized areas as calculated (via equation (2)) directly from the CTH simulations, while the straight lines are the best fit power laws. The right column plots the root mean square of the logarithm (base 10) of the residuals between the calculated areas and the best fit as a function  $\beta$  of and  $P_0$ .

Lillis *et al.* [2010] and shown with light gray horizontal lines in Figure 7) can result from a substantial range of impact energies, spanning more than an order of magnitude, depending upon the pressure-demagnetization properties of the magnetization carrier.

### 3.4. Empirical Model of Impact Demagnetization at Mars

[54] We can utilize the results of these hydrocode simulations to make an empirical model of impact demagnetization at Mars. By fitting the parameters of such a model, we can derive an equation relating demagnetized area to impact energy and pressure-demagnetization parameters  $\beta$  and  $P_0$ , for each Curie temperature  $T_c$ . Demagnetized area  $A$  has a power law dependence on impact energy  $E$ :

$$A = C(\beta, P_0, T_c) E^{q(\beta, P_0, T_c)} \quad (4)$$

where  $C$  is a scaling parameter and  $q$  is the exponent, both dependent upon  $\beta$  and  $P_0$ . The surfaces representing  $C$  and  $q$  as a function of  $\beta$  and  $P_0$  for each value of  $T_c$ , are fit very well

by separate two-dimensional fifth-order polynomials in  $\beta$  and  $P_0$ , where  $k$  and  $g$  are matrices of polynomial coefficients.

$$\log_{10} C(\beta, P_0) = \sum_{i=0}^5 \sum_{j=0}^5 k_{ij} \beta^i P_0^j \quad (5)$$

$$q(\beta, P_0) = \sum_{i=0}^5 \sum_{j=0}^5 g_{ij} \beta^i P_0^j \quad (6)$$

[55] Appendix B contains best fit matrices  $k$  and  $g$  as well as plots of the surfaces of  $C$  and  $q$  as a function of  $\beta$  and  $P_0$ .

[56] Equations (4)–(6) and Tables 3 and 4 (values of matrices  $k$  and  $g$ ) define an empirical function that can be used to calculate the effective demagnetized area resulting from an impact on Mars of a given energy  $E$  into a crust whose magnetic carrier has a Curie temperature of 325°, 580°, or 670° and a pressure-demagnetization curve defined by equation (1) with  $P_{\text{scale}} = 2$  GPa and any given pair of values of  $\beta$  and  $P_0$ . Of course, this empirical model is also subject to the assumptions made for the hydrocode simulations, such as the relative densities of the impactor, crust,

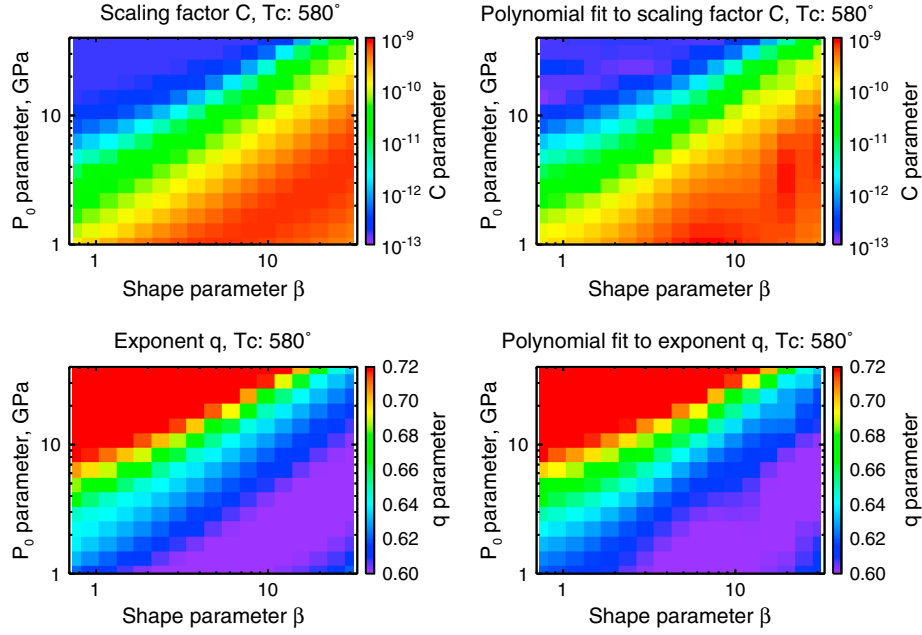


**Figure B2.** The left column shows the best fit values of scale factor  $C$  and exponent  $q$  as a function of  $\beta$  and  $P_0$  for a Curie temperature of  $580^\circ\text{C}$  (magnetite). The right column shows the polynomial fits to those surfaces. Plots for other Curie temperatures look similar and are not shown.

and mantle, as well as the assumed heat flow and thermal conductivity and the impact velocity of 10.6 km/s. For example, slower velocities for the same impact energy may produce relatively more heat from plastic deformation of crust and relatively lower shock heating and peak shock pressures. However, it should nonetheless be a useful tool for studying impact demagnetization.

### 3.5. Impact Demagnetization Bounds for Candidate Minerals

[57] Lastly, we wish to use this framework to attempt to constrain the total demagnetized area as a function of impact

energy for specific candidate Martian magnetic minerals. For each of our seven sample pressure-demagnetization data sets and the best fits of equation (1) to those data sets, we consider the 1-sigma error ellipsoid in the two-dimensional parameter space defined by  $\beta$  and  $P_0$  (see Figure A1). Then, for each impact energy and for the appropriate Curie temperature (e.g.,  $325^\circ\text{C}$  for SD pyrrhotite), we calculate the total demagnetized area for every combination of  $\beta$  and  $P_0$  within the ellipsoid, i.e., the family of “good” fits of equation (1) to each data set. The minimum and maximum values within this ellipsoid form the upper and lower bounds of demagnetized area, subject to the assumption that the true

**Table 3.** Values of  $k_{i,j}$  (See Equation (4) and Appendix B)

$T_c = 325^\circ\text{C}$	$i=0$	$i=1$	$i=2$	$i=3$	$i=4$	$i=5$
$j=0$	-9.245e+00	-1.410e+00	1.639e-01	-8.238e-03	1.874e-04	-1.586e-06
$j=1$	2.417e-01	4.327e-01	-7.684e-02	4.535e-03	-1.116e-04	9.853e-07
$j=2$	-4.255e-02	-6.046e-02	1.272e-02	-8.143e-04	2.099e-05	-1.908e-07
$j=3$	2.760e-03	4.189e-03	-9.452e-04	6.315e-05	-1.675e-06	1.553e-08
$j=4$	-8.078e-05	-1.332e-04	3.111e-05	-2.132e-06	5.758e-08	-5.409e-10
$j=5$	8.840e-07	1.553e-06	-3.702e-07	2.578e-08	-7.047e-10	6.679e-12
$T_c = 580^\circ\text{C}$	$i=0$	$i=1$	$i=2$	$i=3$	$i=4$	$i=5$
$j=0$	-9.488e+00	-8.615e-01	3.656e-02	9.651e-04	-7.832e-05	1.078e-06
$j=1$	2.233e-01	2.729e-01	-2.240e-02	-1.195e-04	3.567e-05	-5.747e-07
$j=2$	-2.346e-02	-4.760e-02	5.613e-03	-1.194e-04	-2.521e-06	6.840e-08
$j=3$	6.513e-04	3.919e-03	-5.430e-04	1.887e-05	-9.595e-08	-2.406e-09
$j=4$	2.165e-06	-1.386e-04	2.075e-05	-8.583e-07	1.021e-08	9.715e-12
$j=5$	-2.068e-07	1.729e-06	-2.705e-07	1.219e-08	-1.817e-10	4.903e-13
$T_c = 670^\circ\text{C}$	$i=0$	$i=1$	$i=2$	$i=3$	$i=4$	$i=5$
$j=0$	-1.005e+01	-4.465e-01	-2.195e-02	4.246e-03	-1.583e-04	1.785e-06
$j=1$	5.629e-01	-6.610e-03	2.492e-02	-3.098e-03	1.143e-04	-1.313e-06
$j=2$	-8.319e-02	3.651e-03	-3.672e-03	4.936e-04	-1.926e-05	2.292e-07
$j=3$	5.017e-03	9.052e-05	1.750e-04	-2.979e-05	1.257e-06	-1.558e-08
$j=4$	-1.382e-04	-1.387e-05	-3.116e-06	7.855e-07	-3.605e-08	4.639e-10
$j=5$	1.431e-06	2.610e-07	1.423e-08	-7.623e-09	3.804e-10	-5.062e-12

**Table 4.** Values of  $g_{ij}$  (See Equation (5) and Appendix B)

$T_c = 325^\circ\text{C}$	$i=0$	$i=1$	$i=2$	$i=3$	$i=4$	$i=5$
$j=0$	5.938e-01	4.621e-02	-5.243e-03	2.568e-04	-5.698e-06	4.708e-08
$j=1$	-4.551e-03	-1.600e-02	2.728e-03	-1.579e-04	3.827e-06	-3.337e-08
$j=2$	8.749e-04	2.344e-03	-4.673e-04	2.930e-05	-7.457e-07	6.710e-09
$j=3$	-5.181e-05	-1.663e-04	3.533e-05	-2.312e-06	6.061e-08	-5.572e-10
$j=4$	1.343e-06	5.367e-06	-1.176e-06	7.893e-08	-2.108e-09	1.965e-11
$j=5$	-1.277e-08	-6.337e-08	1.413e-08	-9.629e-10	2.603e-11	-2.450e-13
$T_c = 580^\circ\text{C}$	$i=0$	$i=1$	$i=2$	$i=3$	$i=4$	$i=5$
$j=0$	6.061e-01	2.321e-02	-3.181e-04	-9.048e-05	4.218e-06	-5.168e-08
$j=1$	-5.587e-03	-8.539e-03	5.017e-04	2.543e-05	-1.872e-06	2.642e-08
$j=2$	4.604e-04	1.593e-03	-1.606e-04	1.050e-06	1.870e-07	-3.435e-09
$j=3$	5.214e-06	-1.361e-04	1.702e-05	-4.635e-07	-3.210e-09	1.557e-10
$j=4$	-1.058e-06	4.914e-06	-6.784e-07	2.458e-08	-1.656e-10	-2.484e-12
$j=5$	1.985e-08	-6.225e-08	9.068e-09	-3.724e-10	4.346e-12	5.963e-15
$T_c = 670^\circ\text{C}$	$i=0$	$i=1$	$i=2$	$i=3$	$i=4$	$i=5$
$j=0$	6.061e-01	2.321e-02	-3.181e-04	-9.048e-05	4.218e-06	-5.168e-08
$j=1$	-5.587e-03	-8.539e-03	5.017e-04	2.543e-05	-1.872e-06	2.642e-08
$j=2$	4.604e-04	1.593e-03	-1.606e-04	1.050e-06	1.870e-07	-3.435e-09
$j=3$	5.214e-06	-1.361e-04	1.702e-05	-4.635e-07	-3.210e-09	1.557e-10
$j=4$	-1.058e-06	4.914e-06	-6.784e-07	2.458e-08	-1.656e-10	-2.484e-12
$j=5$	1.985e-08	-6.225e-08	9.068e-09	-3.724e-10	4.346e-12	5.963e-15

pressure-demagnetization curves for each mineral can be represented by equation (1) beyond measure range down to zero magnetization. Figure 9 demonstrates this fitting for the MD synthetic hematite data from *Bezaeva et al.* [2010], for the case of a 100 km radius impactor.

[58] In this way, we can derive a curve of demagnetized area as a function of impact energy for any mineral for which we know the Curie temperature and at least part of the pressure-demagnetization curve, as shown in Figure 10 for our eight sample data sets. The substantial range in demagnetized area for a given impact energy among our sample of candidate Martian magnetic minerals reflects the diversity of behavior with respect to shock pressures shown in Figure 2. For example, the demagnetized area of the Argyre impact could be caused by impact energies ranging from  $10^{26}$  J to  $\sim 1.5 \times 10^{27}$  J (impactor radii of 50 km to  $\sim 125$  km in our simulations). Similarly, the range of possible impact energies for a basin with a given demagnetized area is approximately an order of magnitude across the range of plausible magnetic minerals.

[59] Unfortunately, due to the substantial variation of pressure-demagnetization characteristics across even different samples of the same mineral (as clearly demonstrated by Figure 4 of *Bezaeva et al.* [2010]), even if we posit a single mineral type as the dominant magnetization carrier in the Martian crust, we are still left with a substantial range of possible energies for a given impact. Conversely, if we posit a specific energy for a known impact, we can constrain the pressure-demagnetization curve reasonably well but, with current information, we still cannot confidently identify the dominant magnetic mineral(s).

#### 4. Conclusions and Future Directions

[60] We have examined the relationship between the impact cratering process and crustal demagnetization on Mars, subject to the validity of the CTH hydrocode model

and the temperature and pressure demagnetization properties of the dominant magnetic carrier. We have shown that in general, shock pressure demagnetization is more important than thermal demagnetization (in agreement with the scaling-law approach of *Mohit and Arkani-Hamed* [2004]), except in the combined case of very large impacts and low Curie temperature minerals such as pyrrhotite. We have also shown that the demagnetized area has a power law dependence on impact energy and that a robust empirical model of that power law dependence for any given magnetic mineral (whose pressure-demagnetization properties are known) can be constructed to enable easier calculation of impact demagnetization on early Mars.

[61] As mentioned in the introduction, most of the previous work on this topic has made use of scaling laws relating impact energy to peak pressure contours and final crater diameter [e.g., *Melosh*, 1989; *Holsapple*, 1993; *Pierazzo et al.*, 1997]. It would be very useful to directly compare peak pressure and temperature contours calculated from the scaling laws with those from hydrocode simulations, varying crust and mantle composition, geothermal gradient, etc., in order to determine the degree to which scaling laws are as viable as results from hydrocode simulations.

[62] Also, the development of an accurate basin scaling law for Mars (i.e., a relationship between basin topography of the surface/Moho and impact energy, which does not currently exist) would greatly complement the techniques developed in this paper. This would allow useful constraints to be placed upon the pressure-demagnetization properties of the dominant magnetic carrier(s), i.e., we could determine which of the curves in Figures 3 and 10 correspond to the Martian case. When combined with (a) extending the range of pressure demagnetization experiments and (b) petrologic constraints from remote sensing of exposed surface minerals and/or meteorite studies, we could then expect to identify the likely primary magnetic mineral(s) and domain state(s) on Mars with some confidence. A corollary is that if the

dominant magnetic mineral is known, these techniques can be used to verify the numerical impact models and associated basin scaling law.

## Appendix A: Fitting Pressure-Demagnetization Behavior of Candidate Minerals

[63] Typical uncertainties in normalized magnetization in shock pressure demagnetization experiments are  $\sim 0.03$  [Bezaeva *et al.*, 2010], which we take to be the measurement error for the purposes of setting equation (1) to the pressure demagnetization data shown in Figure 2. We assume that the scale parameter  $P_{\text{scale}} = 2$  GPa (varying  $P_{\text{scale}}$  or  $\beta$  cause similar effects, as mentioned in section 2.1, so we need not separately vary both). For each of our seven sample data sets, Figure A1 shows the experimental data, the best fit, all fits within the 1-sigma error ellipsoid and the  $\chi^2$  surface, highlighting the error ellipsoid.

[64] We notice a substantial diversity of possible pressure-demagnetization behavior beyond the pressure ranges where data exist, for different minerals. Certain cases, such as MD hematite in granite, show quite a narrow range of possible curves, whereas others such as PSD magnetite in the NWA 998 Nakhilite meteorite show a wide range of possible behavior beyond 1.24 GPa. Of course, these constraints are subject to the implicit assumption that pressure-demagnetization curves are monotonic and can be fully parameterized by equation (1), which would be unable to accommodate any possible breaks or plateaus in the curves.

## Appendix B: Empirical Model for Demagnetized Area

[65] As mentioned in section 3.4, our empirical model assumes that demagnetized area  $A$  has a power law dependence on impact energy  $E$ :

$$A = C(\beta, P_0, T_c) E^{q(\beta, P_0, T_c)} \quad (\text{B1})$$

where  $C$  is a scaling parameter and  $q$  is the exponent, both dependent upon  $\beta$  and  $P_0$ . The left column of Figure B1 shows four sample power law fits, while the right column shows, as a function of  $\beta$  and  $P_0$ , the residuals between (a) the demagnetized area as a function of energy calculated from the CTH simulations and (b) the power law fit to it. The area residuals are quite small, 0.02–0.13 in units of  $\log_{10}(\text{km}^2)$ , showing that a power law is an adequate representation of the relationship between demagnetized area and impact energy.

[66] These best fit values of  $C$  and  $q$  are functions jointly of  $\beta$  and  $P_0$  for each value of  $T_c$ , and are themselves fit very well by separate two-dimensional fifth-order polynomials in  $\beta$  and  $P_0$ :

$$\log_{10} C(\beta, P_0) = \sum_{i=0}^5 \sum_{j=0}^5 k_{ij} \beta^i P_0^j \quad (\text{B2})$$

$$q(\beta, P_0) = \sum_{i=0}^5 \sum_{j=0}^5 g_{ij} \beta^i P_0^j \quad (\text{B3})$$

where  $k$  and  $g$  are matrices of polynomial coefficients.

[67] Figure B2 shows these functions  $C$  and  $q$  (left column) and the polynomial fit to them (right column), for just the Curie temperature of magnetite and shows that these two-dimensional fits also have low residuals. Tables 3

and 4 provides the  $k$  and  $g$  matrices of best fit polynomial coefficients respectively.

[68] **Acknowledgments.** We would like to thank an anonymous reviewer for helpful comments and Jerome Gattacceca, whose comments greatly improved the rock magnetism in the paper. We would also like to thank David Dunlop for useful discussions. This work was supported by the NASA Mars Data Analysis Program (grants NNX07AN94G and NNX11AI85G) and the Mars Fundamental Research Program (grant NNX09AN18G).

## References

- Acuña, M. H., et al. (1999), Global distribution of crustal magnetization discovered by the Mars Global Surveyor MAG/ER experiment, *Science*, 284, 790–793.
- Acuña, M. H., et al. (2001), Magnetic field of Mars: Summary of results from the aerobraking and mapping orbits, *J. Geophys. Res.*, 106, 23403–23417.
- Arkani-Hamed, J., and D. Boutin (2012), Low-magnetic crust underlying province of Mars 217, 209–230, doi:10.1016/j.icarus.2011.10.023.
- Barnes, J., and P. Hut (1986), A hierarchical O(N-log-N) force-calculation algorithm, *Nature*, 324(6096), 446–449.
- Benz, W., A. G. W. Cameron, and H. J. Melosh (1989), The origin of the Moon and the Single-Impact Hypothesis III, 81(1), 113–131.
- Bertelsen, P., et al. (2004), Magnetic properties experiments on the Mars Exploration Rover Spirit at Gusev Crater, *Science*, 305, 827–829, doi:10.1126/science.1100112.
- Bezaeva, N. S., P. Rochette, J. Gattacceca, R. A. Sadykov, V. I. Trukhin (2007), Pressure demagnetization of the Martian crust: Ground truth from SNC meteorites, *Geophys. Res. Lett.*, 34, L23202, doi:10.1029/2007GL031501.
- Bezaeva, N. S., J. Gattacceca, P. Rochette, R. A. Sadykov, and V. I. Trukhin (2010), Demagnetization of terrestrial and extraterrestrial rocks under hydrostatic pressure up to 1.2 GPa, *Phys. Earth Planet. Inter.*, 179, 7–20, doi:10.1016/j.pepi.2010.01.004. This.
- Borradaile, G. J., and M. Jackson (1993), Changes in magnetic remanence during simulated deep sedimentary burial, *Phys. Earth Planet. Int.*, 77, 315–327, doi:10.1016/0031-9201(93)90106-J.
- Canup, R. M., and E. Asphaug (2001), Origin of the Moon in a giant impact near the end of the Earth's formation, *Nature*, 412(6848), 708–712, doi:10.1038/35089010.
- Canup, R. M., and A. C. Barr (2010), Modeling moon-forming impacts: High-resolution SPH and CTH simulations, *Lunar & Planet. Sci. Conf.*, 41, Abs. 2488.
- Christensen, P. R., et al. (2000), Detection of crystalline hematite mineralization on Mars by the Thermal Emission Spectrometer: Evidence for near-surface water, *J. Geophys. Res.*, 105(E4), 9623–9642, doi:10.1029/1999JE001093.
- Cisowski, S. M., and M. Fuller (1978), The Effect of Shock on the Magnetism of Terrestrial Rocks, *J. Geophys. Res.*, 83(B7), 3441–3458, doi:10.1029/JB083iB07p03441.
- Cisowski, S. M., J. R. Dunn, M. Fuller, Y. Wu, M. F. Rose, P. J. Wasilewski, (1976), Magnetic effects of shock and their implications for lunar magnetism (II), *Lunar Science Conference*, 7th, Houston, Tex., March 15–19, 1976. Proceedings 3, 3299–3320.
- Connerney, J. E. P., M. H. Acuña, P. J. Wasilewski, G. Kletetschka, N. F. Ness, H. Rème, R. P. Lin, and D. L. Mitchell (2001), The global magnetic field of Mars and implications for crustal evolution, *Geophys. Res. Lett.*, 28(21), 4015–4018, doi:10.1029/2001GL013619.
- Crawford, D. A. (2010), Parallel N-body gravitational interaction in CTH for planetary defense and large impact simulations, *Int. J. Impact Eng.* (Proceedings of the 11th Hypervelocity Impact Symposium), accepted.
- Crawford, D. A., and M. E. Kipp (2010), Giant impact theory for origin of the Moon: High resolution CTH simulations, *Lunar & Planet. Sci. Conf.*, 41, Abs. 1405.
- Dekkers, M. J. (1989), Magnetic properties of natural pyrrhotite. II. High- and low-temperature behavior of  $J_s$  and TRM as function of grain size, *Phys. Earth Planet. Int.*, 57, 266–283, doi:10.1016/0031-9201(89)90116-7.
- Dunlop, D. J. (2009), Continuous and stepwise thermal demagnetization: are they equivalent?, *Geophys. J. Int.*, 177, 949–957, doi:10.1111/j.1365-246X.2009.04152.x.
- Dunlop, D. J., and J. Arkani-Hamed (2005), Magnetic minerals in the Martian crust, *J. Geophys. Res.*, 110, E12S04, doi:10.1029/2005JE002404.
- Dunlop, D. J., and O. Ozdemir (1997), *Rock Magnetism: Fundamentals and Frontiers*, pp. 69–70, Cambridge University Press, Cambridge, U. K.
- Feinberg, J. M., H.-R. Wenk, P. R. Renne, and G. R. Scott (2004), Epitaxial relationships of clinopyroxene-hosted magnetite determined using electron backscatter diffraction (EBSD) technique, *Am. Mineral.*, 89, 462–466.
- Frey, H. V. (2006), Impact constraints on, and a chronology for, major events in early Mars history, *J. Geophys. Res.*, 111, E08S91, doi:10.1029/2005JE002449.

- Frey, H. V. (2008), Ages of very large impact basins on Mars: Implications for the late heavy bombardment in the inner solar system, *Geophys. Res. Lett.*, *35*, L13203, doi:10.1029/2008GL033515.
- Gattacceca, J., M. Boustie, B. P. Weiss, P. Rochette, E. A. Lima, L. E. Fong, and F. J. Baudenbacher (2006), Investigating impact demagnetization through laser impacts and SQUID microscopy, *Geology*, *34*, 333–336, doi:10.1130/G21898.1.
- Gattacceca, J., L. Berthe, M. Boustie, F. Vadeboin, P. Rochette, and T. De Resseguier (2007a), On the efficiency of shock remanent processes, *Phys. Earth Planet. Inter.*, doi:10.1016/j.pepi.2007.1009.1005.
- Gattacceca, J., A. Lamali, P. Rochette, M. Boustie, and L. Berthe (2007b), The effects of explosive-driven shocks on the natural remanent magnetization and the magnetic properties of rocks, *Phys. Earth Planet. Inter.*, *162*, 85–98, doi:10.1016/j.pepi.2007.1003.1006.
- Gattacceca, J., M. Boustie, E. Lima, T. de Resseguier, and J. P. Cuq-Lelandais (2010), Unraveling the simultaneous shock magnetization and demagnetization of rocks, *Phys. Earth Planet. Inter.*, *182*, 42–49, doi:10.1016/j.pepi.2010.06.009.
- Gilder, S. A., M. Le Goff, and J.-C. Chervin (2006), Static stress demagnetization of single and multi-domain magnetite with implications for meteorite impacts, *High Pressure Res.*, *26*, 539–547, doi:10.1080/08957950601092085.
- Hargraves, R. B., J. M. Knudsen, P. Bertelsen, W. Goetz, H. P. Gunnlaugsson, S. F. Hviid, M. B. Madsen, and M. Olsen (2000), Magnetic enhancement on the surface of Mars?, *J. Geophys. Res.*, *105*(E1), 1819–1827, doi:10.1029/1999JE001032.
- Hartmann, W. K., and G. Neukum (2001), Cratering chronology and the evolution of Mars, *Space Sci. Rev.*, *96*, 165–194.
- Hauk, S. A., and R. J. Phillips (2002), Thermal and crustal evolution of Mars, *J. Geophys. Res.-Planets*, *107*(E7), 5052, doi:10.1029/2001je001801.
- Holsapple, K. A. (1993), The scaling of impact processes in planetary sciences, *Annu. Rev. Earth Planet. Sci.*, *21*, 333–373.
- Hood, L. L., N. C. Richmond, E. Pierazzo, and P. Rochette (2003), Distribution of crustal magnetic fields on Mars: Shock effects of basin-forming impacts, *Geophys. Res. Lett.*, *30*(6), 1281, doi:10.1029/2002GL016657.
- Hood, L. L., K. P. Harrison, B. Langlais, R. J. Lillis, F. Poulet, and D. A. Williams (2010), Magnetic anomalies near Apollinaris Patera and the Medusae Fossae Formation in Lucas Planum, Mars, *Icarus*, *208*(1), 118–131, doi:10.1016/j.icarus.2010.01.009.
- Ivanov, B. A., H. J. Melosh, and E. Pierazzo (2010), Basin-forming impacts: Reconnaissance modeling in *Large Meteorite Impacts and Planetary Evolution IV*, edited by R. L. Gibson, and W. U. Reimold, pp. 29–49, Geological Society of America.
- Kerley, G. I. (1993), Multiphase equation of state for iron, Technical Report SAND93-0027, 64 pp, Sandia National Laboratory, Albuquerque, N.M.
- Kletetschka, G., J. E. P. Connerney, N. F. Ness, and M. H. Acuna (2004), Pressure effects on Martian crustal magnetization near large impact basins, *Meteorit. Planet. Sci.*, *39*(11), 1839–1848.
- Lillis, R. J., H. V. Frey, M. Manga, D. L. Mitchell, R. P. Lin, M. H. Acuña, and S. W. Bougher (2008a), An improved crustal magnetic field map of Mars from electron reflectometry: Highland volcano magmatic history and the end of the Martian dynamo, *Icarus*, *194*, 575–196.
- Lillis, R. J., H. V. Frey, and M. Manga (2008b), Rapid decrease in Martian crustal magnetization in the Noachian era: Implications for the dynamo and climate of early Mars, *Geophys. Res. Lett.*, *35*, L14203, doi:10.1029/2008GL034338.
- Lillis, R. J., M. E. Purucker, J. S. Halekas, K. L. Louzada, S. T. Stewart-Mukhopadhyay, M. Manga, and H. V. Frey (2010), Study of impact demagnetization at Mars using Monte Carlo modeling and multiple altitude data, *J. Geophys. Res.*, *115*, E07007, doi:10.1029/2009JE003556.
- Louzada, K. L., Stewart, S. T. (2009), Effects of planet curvature and crust on the shock pressure field around impact basins, *Geophys. Res. Lett.*, *36*, L15203, doi:10.1029/2009GL037869.
- Louzada, K. L., S. T. Stewart, B. P. Weiss, J. Gattacceca, and N. S. Bezaeva (2010), Shock and static pressure demagnetization of pyrrhotite and implications for the Martian crust, *Earth Planet. Sci. Lett.*, *290*, 90–101, doi:10.1016/j.epsl.2009.12.006.
- Louzada, K. L., S. T. Stewart, B. P. Weiss, J. Gattacceca, R. J. Lillis, and J. S. Halekas (2011), Impact demagnetization of the Martian crust: Current knowledge and future directions, *Earth Planet. Sci. Lett.*, *305*, 257–269, doi:10.1016/j.epsl.2011.03.013.
- McEnroe, S. A., L. L. Brown, and P. Robinson (2004), Earth analog for Martian magnetic anomalies: Remanence properties of hemo-ilmenite norites in the Bjerkreim-Sokndal intrusion, Rogaland, Norway, *J. Appl. Geophys.*, *56*, 3, 195–212, doi:10.1016/j.jappgeo.2004.07.002.
- McGlaun, J. M., S. L. Thompson, and M. G. Elrick (1990), CTH: A 3-dimensional shock-wave physics code, *Int. J. Impact Eng.*, *10*, 351–360, doi:10.1016/0734-743X(90)90071-3.
- McSween, H. Y., Jr., T. L. Grove, and M. B. Wyatt (2003), Constraints on the composition and petrogenesis of the Martian crust, *J. Geophys. Res.*, *108*(E12), 5135, doi:10.1029/2003JE002175.
- Melosh, H. J. (1989), *Impact Cratering: A Geologic Process*, pp. 17–25, Oxford Univ. Press, New York.
- Melosh, H. J. (2007), A hydrocode equation of state for SiO<sub>2</sub>, *Meteorit. Planet. Sci.*, *42*(12), 2079–2098.
- Mitchell, D. L., R. J. Lillis, R. P. Lin, J. E. P. Connerney, and M. H. Acuña (2007), A global map of Mars' crustal magnetic field based on electron reflectometry, *J. Geophys. Res.*, *112*, E01002, doi:10.1029/2005JE002564.
- Mohit, P. S., and J. Arkani-Hamed (2004), Impact demagnetization of the Martian crust, *Icarus*, *168*, 305–317.
- Neumann, G. A., M. T. Zuber, M. A. Wieczorek, P. J. McGovern, F. G. Lemoine, and D. E. Smith (2004), Crustal structure of Mars from gravity and topography, *J. Geophys. Res.*, *109*, E08002, doi:10.1029/2004JE002262.
- Neumann, G. A., M. T. Zuber, F. G. Lemoine, D. E. Smith (2008), Crustal thickness inversions from recent Mars Reconnaissance Orbiter gravity solutions, COSPAR July 18, 2008, Montreal, Canada.
- Nimmo, F., and K. Tanaka (2005), Early crustal evolution of Mars, *Annu. Rev. Earth Planet. Sci.*, *33*, 133–161, doi:10.1146/annurev.earth.33.092203.122637.
- Ogawa, Y., and M. Manga (2007) Thermal demagnetization of Martian upper crust by magma intrusion, *Geophys. Res. Lett.*, *34*, L16302, doi:10.1029/2007GL030565.
- Ozdemir, O., and D. J. Dunlop (2005), Thermoremanent magnetization of multidomain hematite, *J. Geophys. Res.*, *110*, B09104, doi:10.1029/2005JB003820.
- Pierazzo, E., A. M. Vickery, and H. J. Melosh (1997), A reevaluation of impact melt production, *Icarus*, *127*, 408–423.
- Pierazzo, E., et al. (2008), Validation of numerical codes for impact and explosion cratering: Impacts on strengthless and metal targets, *Meteorit. Planet. Sci.*, *43*, 1917–1938.
- Rochette, P., J. P. Lorand, G. Fillion, and V. Sautter (2001), Pyrrhotite and the remanent magnetization of SNC meteorites: A changing perspective on Martian magnetism, *Earth Planet. Sci. Lett.*, *190*, 1–12.
- Rochette, P., G. Fillion, R. Ballou, F. Brunet, B. Ouladdiaf, and L. Hood (2003), High pressure magnetic transition in pyrrhotite and impact demagnetization on Mars, *Geophys. Res. Lett.*, *30*(13), 1683, doi:10.1029/2003GL017359.
- Saar, M. O., and M. Manga (2004), Depth dependence of permeability in the Oregon Cascades inferred from hydrogeologic, thermal, seismic, and magmatic modeling constraints, *J. Geophys. Res.*, *109*, B04204, doi:10.1029/2003JB002855.
- Schultz, P. H., and D. A. Crawford (2008), Consequences of Forming the South-Pole-Aitken Basin, Lunar & Planet. Sci. Conf., 39, Abs. 2451.
- Scott, E., and M. Fuller (2004), A possible source for the Martian crustal magnetic field, *Earth Planet. Sci. Lett.*, *220*, 83–90, doi:10.1016/S0012-821X(04)00032-9.
- Senft, L. E., and S. T. Stewart (2007), Modeling impact cratering into layered surfaces, *J. Geophys. Res.*, *112*, E11002, doi:10.1029/2007JE002894.
- Senft, L. E., and S. T. Stewart (2009), Dynamic fault weakening and the formation of large impact craters, *Earth Planet. Sci. Lett.*, *287*, 471–482, doi:10.1016/j.epsl.2009.08.033.
- Shahnas, H., and J. Arkani-Hamed (2007), Viscous and impact demagnetization of Martian crust, *J. Geophys. Res.*, *112*, E02009, doi:10.1029/2005JE002424.
- Smith, D. E., et al. (2001), Mars Orbiter Laser Altimeter: Experiment summary after the first year of global mapping of Mars, *J. Geophys. Res.*, *106*(E10), 23,689–23,722, doi:10.1029/2000JE001364.
- Springel, V. (2005), The cosmological simulation code GADGET-2, *Mon. Not. R. Astron. Soc.*, *364*(4), 1105–1134, doi:10.1111/j.1365-2966.2005.09655.x.
- Stewart, S. T. (2011), Impact basin formation: The mantle excavation paradox resolved, *Lunar Planet. Sci. Conf.*, *42*, 1633.
- Stewart, S. T. (2012), Impact basin formation and structure from 3D simulations, Lunar & Planet. Sci. Conf., 43, Abs. 2865.
- Stokking, L. B., and L. Tauxe (1987), Acquisition of chemical remanent magnetization by synthetic iron oxide, *Nature*, *327*, 610–612, doi:10.1038/327610a0.
- Whittington, A. G., A. M. Hofmeister, and P. I. Nabalek (2009), Temperature-dependent thermal diffusivity of Earth's crust and implications for magmatism, *Nature*, *458*, 319–321.
- Wieczorek, M. A., B. P. Weiss, and S. T. Stewart (2012), An impactor origin for lunar magnetic anomalies, *Science*, *335*, 1212–1215.
- Zhang, J. Z., and C. Herzberg (1994), Melting KLB-1 from 5.0 to 22.5 GPa, *J. Geophys. Res.*, *99*(B9), 17729–17742.
- Zucker, R. V., and S. T. Stewart (2010), Fault weakening and shear localization during crater collapse, Lunar & Planet. Sci. Conf., 41, Abs. 2722.